



Revised chronostratigraphy of DSDP Site 270 and late Oligocene to early Miocene paleoecology of the Ross Sea sector of Antarctica

Denise K. Kulhanek^{a,*}, Richard H. Levy^b, Christopher D. Clowes^b, Joseph G. Prebble^b, Daniel Rodelli^c, Luigi Jovane^c, Hugh E.G. Morgans^b, Christoph Kraus^d, Horst Zwingmann^e, Elizabeth M. Griffith^f, Howie D. Scher^g, Robert M. McKay^d, Timothy R. Naish^d

^a International Ocean Discovery Program, Texas A&M University, 1000 Discovery Drive, College Station, TX 77845, USA

^b GNS Science, PO Box 30368, Lower Hutt 5040, New Zealand

^c University of São Paulo, São Paulo, SP 05508-120, Brazil

^d Antarctic Research Centre, Victoria University of Wellington, Wellington, New Zealand

^e Department of Geology and Mineralogy, Kitashirakawa Oiwakecho, Sakyo-ku, Kyoto University, Kyoto 606-8502, Japan

^f The Ohio State University, Columbus, OH 43210, USA

^g University of South Carolina, Columbia, SC 29208, USA

ARTICLE INFO

Keywords:

Ross Sea

DSDP Site 270

Chronostratigraphy

Magnetostratigraphy

Biostratigraphy

Paleoecology

ABSTRACT

Deep Sea Drilling Project (DSDP) Site 270, located in the central high of the Ross Sea, was cored to 422.5 m below seafloor (mbsf) and recovered a thick Oligocene to lower Miocene sequence of mudstone with varying amounts of ice rafted debris (IRD), overlain by ~20 m of Pliocene to Recent diatom silty clay with IRD. This site provides important temporal constraints on regional stratigraphy and insights into late Oligocene to early Miocene ice sheet dynamics; however, previous age models were based on limited data. Here we provide a revised age model using a combination of biostratigraphy (dinoflagellate cysts, pollen, calcareous nannofossils, foraminifers, and diatoms), magnetostratigraphy, Sr-isotope stratigraphy, and K–Ar dating of glauconite. We divide the sequence between 386 and 20 mbsf into four chronostratigraphic intervals (CSIs). CSI 1 (386–352 mbsf) is dated to between ~26 and 25 Ma based on glauconite K–Ar dating, the highest occurrence (HO) of the dinoflagellate *Lejeunecysta rotunda* (24.5 Ma), and a paleomagnetic reversal tied to the C8r/C8n.2r boundary (25.987 Ma). A distinct change in the benthic foraminifer assemblage at 352 mbsf marks an unconformity and the base of CSI 2. CSI 2 (352 to 149–146 mbsf) is dated to between 25.44 Ma and 23.13 Ma based on nannofossil biostratigraphy. Within this 200 m interval we correlate seven magnetic reversals to Chrons C8n.2n to C6Cr (25.3–23.3 Ma) and our line of correlation suggests rapid sedimentation (~80 m/m.y.). Microfossil and lithologic evidence indicate a distal marine setting with a paleo-water depth of ~200 m at 345 mbsf, with deepening above. Within CSI 2 is a diamictite overlain by grounding line proximal sandstone and laminated mudstone indicating glaciomarine deposition in a grounding-line proximal setting between 245 and 230 mbsf, followed by ice sheet grounding-line retreat into a more distal setting from 230 to 146 mbsf (~24.5–23.5 Ma), likely due to basin subsidence and incursion of relatively warm deep water onto the shelf. Another unconformity between 149 and 146 mbsf marks the boundary between CSI 2 and CSI 3. The thin CSI 3 (149–146 to 121/112 mbsf) is dated to ~23 Ma and we place the Oligocene/Miocene boundary at the base of the sequence, although we cannot rule out that the boundary is represented by an unconformity. Benthic foraminifers indicate continued deepening in the earliest Miocene and finer-grained mudstone with less IRD suggests that the site remained in a grounding line distal setting, although a decrease in abundance of calcareous plankton indicates cooling climatic conditions at that time. The boundary between CSI 3 and CSI 4 is marked by an unconformity spanning at least 2.5 m.y. based on the lowest occurrence of the dinoflagellate *Batiacasphaera cooperi* (< 20.7 Ma) at 111 mbsf. Biostratigraphic data constrain CSI 4 to the early Miocene. We tentatively identify three magnetic reversals within CSI 4 (121/112–20 mbsf) that may tie this interval to Chrons C6An.2n to C6r (~20.6–19.7 Ma). A major unconformity at 20 mbsf separates the lower Miocene sediments from the

* Corresponding author.

E-mail address: kulhanek@iodp.tamu.edu (D.K. Kulhanek).

<https://doi.org/10.1016/j.gloplacha.2019.04.002>

Received 23 May 2018; Received in revised form 18 March 2019; Accepted 3 April 2019

Available online 05 April 2019

0921-8181/ © 2019 Elsevier B.V. All rights reserved.

overlying Pliocene and younger sediments. Late Oligocene to early Miocene pollen assemblages from Site 270 suggest a tundra landscape with low-growing *Nothofagaceae*, *Podocarpaceae*, and *Proteaceae* scrub in warmer locations with a relatively stable terrestrial environment during that time.

1. Introduction

Our understanding of Antarctic climate evolution has increased substantially over the last five decades, due primarily to analysis of rock and sediment cores collected from below the circum-Antarctic seafloor. Despite the importance of Antarctica's role in past, present, and future climate, there are few proximal records available due to the expense and difficulty of conducting drilling campaigns in the Antarctic region. On the other hand, there is a wealth of seismic data available around Antarctica that is the basis for much of our understanding. However, these geophysical data need to be tied to geologic sections so that seismic reflectors can be dated (e.g., [Henrys et al., 2001](#); [Wilson et al., 2012](#)). Recovering in situ rocks also allows for detailed lithofacies

analyses that increase our understanding of the waxing and waning of the Antarctic ice sheets through the Cenozoic (e.g., [Bartek and Anderson, 1991](#); [Powell et al., 1998](#); [Barrett, 2007](#); [Naish et al., 2009](#); [Fielding et al., 2011](#); [Passchier et al., 2011](#); [Patterson et al., 2014](#)).

Legacy cores from around the Antarctic continent are a valuable resource that can help advance our understanding of Antarctic and Southern Ocean climate evolution (e.g., [Hassold et al., 2009](#); [Cook et al., 2014](#); [Golledge et al., 2017](#); [Huck et al., 2017](#)). Ross Sea cores collected during Deep Sea Drilling Project (DSDP) Leg 28 were the first deep sea cores collected from the Antarctic, with some of the highest recovery rates for the Antarctic continental shelf, making them a valuable resource. However, regional chronostratigraphic data were rare at the time these cores were recovered, which limited development of

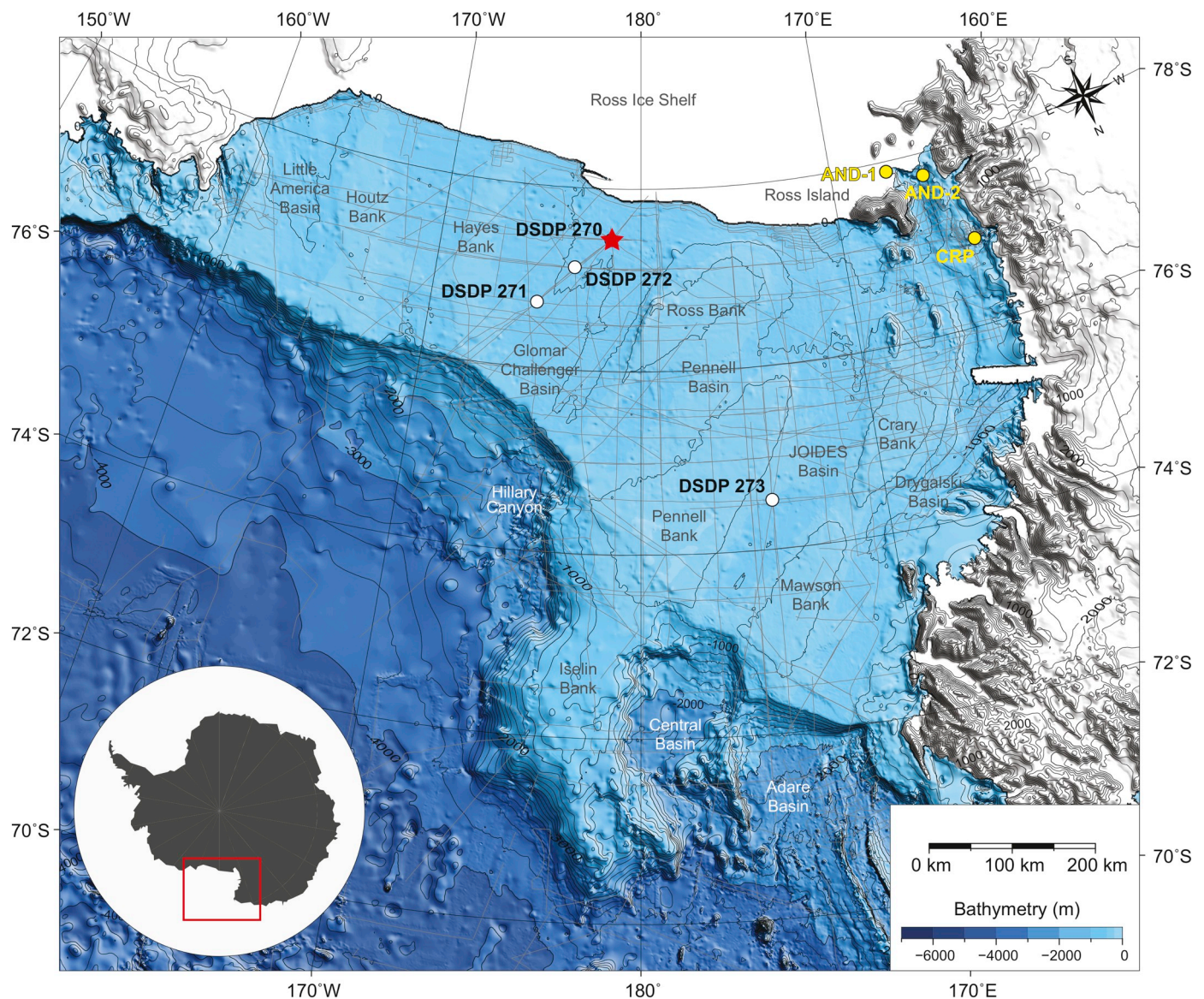


Fig. 1. Location map showing regional overview of Ross Sea area, Deep Sea Drilling Project (DSDP) Site 270, other sites mentioned in the text (DSDP, Cape Roberts Project [CRP], CIROS, ANDRILL), and seismic profile network (grey lines). DSDP Site 270 denoted by a star, other sites by dots. Inset map shows location of regional map on the Antarctic continent. Ross Sea bathymetry is from the International Bathymetric Chart of the Southern Ocean ([Arndt et al., 2013](#)). Existing seismic network is from the Antarctic Seismic Data Library System and includes some single-channel seismic profiles.

robust age models for the sites at the time they were collected. Over the last four decades, there have been significant improvements in Southern Ocean chronostratigraphic methods (e.g., Cody et al., 2008, 2012; Persico et al., 2012; Clowes et al., 2016; Bijl et al., 2018) that can now be applied to these legacy cores so that they can be used to address contemporary paleoclimatic questions. Antarctic paleoclimate data are particularly important now as climate and ice sheet modelers attempt to validate their models and improve projections of future Antarctic ice sheet dynamics (e.g., Golledge et al., 2015; Pollard et al., 2015; DeConto and Pollard, 2016).

Far-field deep sea isotope records suggest that the Oligocene/Miocene transition is characterized by an increase in Antarctic ice volume (e.g., Miller et al., 1991; Zachos et al., 1997; Lear et al., 2004). Yet, there are very few ice-sheet proximal records through this interval to test this hypothesis and of these records, the majority have been collected from the Ross Sea sector of the Southern Ocean. The CIROS-1 and Cape Roberts Project (CRP) 2/2A drill cores are well dated and have been used in numerous studies to further our understanding of Antarctic climate evolution and East Antarctic Ice Sheet variations (e.g., Barrett et al., 1991; Powell et al., 1998; Wilson et al., 1998; Naish et al., 2001; Roberts et al., 2003; Passchier and Krissek, 2008; Wilson et al., 2009). Deep Sea Drilling Project (DSDP) Site 270 is unique as it recovered an upper Oligocene to lower Miocene record of West Antarctic Ice Sheet (WAIS) advance and retreat in the central Ross Sea (Hayes et al., 1975). However, detailed climatic studies have been hampered by a poorly resolved age model that was last refined in the 1980s (Leckie and Webb, 1986).

Herein we present a revised chronostratigraphy based on a combination of biostratigraphy from multiple fossil groups, magnetostratigraphy, radiometric dating of glauconite, and Sr-isotope stratigraphy. We also use microfossil assemblages and lithofacies to assess paleoenvironmental change. This revised chronostratigraphy provides a framework for studies of Antarctic glacial evolution during the late Oligocene to early Miocene at this ice-proximal site.

2. Geological setting

2.1. Ross Sea geology and seismic stratigraphy

The southern Ross Sea consists of 3 sedimentary basins (Victoria Land Basin [VLB], Central Trough [CT], Eastern Basin [EB]) separated by the Coulman and Central Highs (Cooper et al., 1991). Hinz and Block (1984) identified 6 major seismic unconformities (1–6) in the Eastern Basin. Brancolini et al. (1995) correlated these unconformities across the Ross Sea and renamed them Ross Sea Unconformities (RSU) 1–6. They also included an additional major unconformity (4a) identified by Cooper et al. (1991). These unconformities separate eight seismic sequences (Ross Sea seismic sequences [RSS] 1–8) that record the evolution of the Antarctic Ice Sheets since at least 34 Ma (Eocene/Oligocene boundary).

2.2. Summary of earlier work

DSDP Site 270 is located on the central high of the Ross Sea (77° 26.48'S, 178° 30.19'W) in 633 m of water (Fig. 1). The site was continuously rotary cored to 422.5 m below seafloor (mbsf) in early 1973, with 62% core recovery (Hayes et al., 1975). The uppermost ~20 mbsf consists of Pliocene to Recent glacial deposits [diatom-bearing mudstone with ice-rafted debris (IRD) (granules and pebbles)], which are underlain by a thick sequence (20–385 mbsf) of more indurated glacial deposits (mudstone with clasts) of Oligocene to early Miocene age. Below the glacial mudstone is a calcareous glauconitic sandstone unit (~1 m thick) and a 2 m thick carbonaceous sandstone with woody fragments, which is underlain by a sedimentary breccia with metamorphic and granitic clasts that is extensively weathered in the upper 3 m and is inferred to represent a regolith deposit. A nonconformity

separates the sedimentary breccia above from basement composed of grey marble and gneiss below. The basement is thought to be early Paleozoic in age (Shipboard Scientific Party, 1975).

Samples were examined shipboard and onshore following the end of the cruise for foraminifers, calcareous nannofossils, diatoms, radiolarians, and palynomorphs (including pollen, spores, dinoflagellates, and acritarchs). Chen (1975) reported radiolarians were present only as fragments, except in the Pleistocene sediment of Core 1R, which contains a few well-preserved specimens that are younger than Miocene in age. McCollum (1975) similarly reported that diatoms are only present in samples from Core 1R and absent below. However, later analysis found one sample (13R-3, 110–112 cm) with a rich diatom assemblage that includes *Kisseleviella carina* (Steinhauff et al., 1987). Some morphotypes of this taxon were split into a new species, *K. tricornata*, by Olney et al. (2005), including the specimens found from Site 270 (D. Harwood, personal communication). Bukry (1975) examined three samples but did not find calcareous nannofossils. Burns (1975) found nannofossil specimens in two samples from Cores 18R and 22R that comprise a sparse assemblage of *Reticulofenestra* spp. and *Cyclargolithus floridanus*, indicating an Oligocene to Miocene age. Marie-Pierre Aubry later examined ten samples, with one from Core 18R yielding a reasonably diverse assemblage. She assigned it an early Miocene age based on the presence of *Helicosphaera* cf. *H. carteri*, *Cyclococcolithes* (= *Calcidiscus*) *macintyreii*, and *Sphenolithus moriformis/neoabies* (Leckie and Webb, 1986). She considered specimens of *Reticulofenestra bisecta* reworked.

Benthic foraminifers provided the best age constraints following the end of the cruise, indicating an Oligocene age for Cores 34R and deeper based on the presence of taxa known from the Oligocene of New Zealand, including *Chiloguembelina cubensis* and *Gyroidinoides* specimens similar to New Zealand taxa *G. zelandica* and *G. allani*. The Oligocene/Miocene boundary was placed between Sections 34R-CC and 33R-3 (~300 mbsf) based on the presence of *Elphidium* in Section 33R-3 (Shipboard Scientific Party, 1975). Kaneps (1975) noted the presence of a single specimen of *Globigeneroides trilobus* in Core 28R (~253 mbsf), which is known from the Miocene of New Zealand, but suggested that the specimen was a laboratory contaminant. Kemp (1975) also interpreted the dinoflagellate assemblage from the lowermost part of the glaciomarine section (below ~380 mbsf) as Oligocene.

Benthic foraminifers and palynomorph assemblages were also used to make preliminary paleoenvironmental interpretations. Pollen assemblages above the glauconitic sandstone in Cores 41R and 42R reflect cool temperate vegetation (Kemp, 1975). The late Oligocene benthic foraminifer assemblages also show affinities to contemporaneous New Zealand assemblages, suggesting a more temperate influence in the Ross Sea region at that time. On the other hand, the younger part of the section above Core 34R shows more endemism and fewer affinities to New Zealand assemblages, suggesting a shift towards more polar conditions by the latest Oligocene to Miocene (Shipboard Scientific Party, 1975). Overall, the shipboard paleontological results suggested a nearshore depositional environment near the base of the section, with deepening to ~500 m by the early Miocene, and a transition from more temperate to polar conditions over this interval (Shipboard Scientific Party, 1975).

Later work on benthic foraminifers defined four assemblage zones spanning the glaciomarine section and underlying glauconitic sandstone and carbonaceous sandstone units. (Leckie and Webb, 1983, 1986). The *Cyclammina-Ammoscalaria-Anomalinoidea* (C-A-A) Zone (388–352 mbsf) is dominated by agglutinated taxa, with calcareous benthic foraminifers becoming more abundant within the lowermost part of the glaciomarine section. This interval was interpreted to represent a shallow marine setting, with the incursion of calcareous benthic foraminifers indicating deepening (but still < 100 m water depth). The *Globocassidulina-Cassidulinoides-Trochoelphidiella* (G-C-T) Zone (352–196 mbsf) is dominated by calcareous benthic foraminifers near the base that may indicate slightly deeper paleo water depth

(150–300 m). Diversity decreases upsection within this zone, which was interpreted to reflect a change to less stable environmental conditions. The *Haplophragmoides-Trifarina-Cibicides* (H-T-C) Zone (196–121/112 mbsf) represents a gradual change to more abundant agglutinated taxa, although calcareous forms are still present but show more dissolution (Dell and Fleming, 1975). Leckie and Webb (1983, 1986) interpreted this to indicate a change to more corrosive bottom waters. The *Epistominella-Elphidium-Noionella* (E-E-N) Zone (121/112–20 mbsf) represents a change to a low diversity benthic foraminifer fauna that are dissolution-resistant and lacking agglutinated forms. This change was interpreted to reflect further cooling. This assemblage also suggests that water depths above the site were 300–500 m, indicating gradual crustal subsidence occurred in the late Oligocene to early Miocene.

Allis et al. (1975) conducted a magnetostratigraphic study and assigned the interval from 30 to 240 mbsf to the early Miocene (17–22 Ma) based on a similarity to the seafloor magnetic anomaly time scale of Heitzler et al. (1968). They noted that this correlation requires a nearly constant sedimentation rate of 41 m/m.y. Between 240 and 370 mbsf, the sediment is normally magnetized, likely due to the presence of authigenic minerals that are magnetically unstable. However, they used the constant sedimentation rate to place the Oligocene/Miocene boundary at ~260 mbsf, somewhat shallower than indicated by foraminifers (Shipboard Scientific Party, 1975; Leckie and Webb, 1983, 1986). A sample of glauconite from the glauconitic sandstone at 385–386 mbsf (below the base of the glaciomarine section) was dated using K–Ar radiometric dating. The sample was split into two, and the purest one (with minimal clay) yielded a K–Ar age of 26.0 My (McDougall, 1977).

The K–Ar age of 26.0 Ma from the glauconitic sandstone at 385 mbsf constrains the base of the glaciomarine section to late Oligocene. Magnetostratigraphy constrained by the early Miocene age based on benthic foraminifers for the sediment below the angular unconformity at ~20 mbsf suggested an age range of 17–22 Ma for the glaciomarine unit based on comparison to marine magnetic anomalies and extrapolation of a constant sedimentation rate (Allis et al., 1975). Later work by Savage and Ciesielski (1983) indicated an age > 19.2 Ma for the sediment below the angular unconformity based on the seismic stratigraphic relationship to nearby DSDP Site 272 and a diatom-based age for those sediments. The position of the Oligocene/Miocene boundary was placed at either ~300 mbsf based on foraminifers (Shipboard Scientific Party, 1975; Leckie and Webb, 1983, 1986) or ~260 mbsf based on magnetostratigraphy (Allis et al., 1975).

DSDP Site 270 is a rare archive of the Oligocene/Miocene transition in Antarctica, but our ability to make paleoenvironmental interpretations is hampered by the lack of a robust age model. Here we use a multidisciplinary approach to produce a revised age-depth model by combining results from newly collected biostratigraphic, paleomagnetic, radiometric, and isotopic data.

3. This study: materials and methods

Samples for calcareous nannofossil and foraminifer analyses were initially collected from sediment within macrofossils that had been collected from the Site 270 cores and housed in the collections at GNS Science (Lower Hutt, New Zealand). After these samples yielded encouraging results, we collected approximately 180 additional samples from the cores, which are housed at the Gulf Coast Repository, College Station, Texas, USA. Sampling targeted lighter colored intervals and was also guided by the shipboard smear slides results, which noted the presence of various microfossils. We also resampled the glauconitic sandstone at the base of the marine sequence for K–Ar dating. Oriented cubes (approximately 8 cm³) for paleomagnetic analysis were sampled in 2009.

3.1. Paleomagnetism

Natural Remanent Magnetization (NRM) was measured with a 2G Enterprises Long Core Squid Magnetometers housed in shielded rooms at the University of California, Davis (United States) Paleomagnetic Laboratory and Instituto de Astronomia, Geofísica e Ciências Atmosféricas da Universidade de São Paulo (Brazil) Paleomagnetic Laboratory. An alternating field (AF) demagnetization technique was used to remove secondary NRM components, with stepwise demagnetizations of 2.5, 5, 10, 15, 20, 30, 40, 50, 60, 70, 80, 90, and 100 mT. Vector components diagrams (Zijderveld, 1967; Dunlop, 1979) were used to display and evaluate stepwise demagnetization data. The characteristic remanent magnetization (ChRM) directions were determined using stereographic projections and orthogonal and demagnetization intensity plots with the software PuffinPlot (Lurcock and Wilson, 2012). The directions of the ChRM components were then calculated using Principal Component Analysis (PCA; Kirschvink, 1980). Samples were discarded from the final analysis based on the following criteria: (1) low quality for samples with a maximum angular deviation (MAD) > 10°; (2) low inclination for samples with a ChRM inclination shallower than ± 10°; or (3) outlier for single samples that exhibited a ChRM inclination opposite that of the adjacent samples. In addition, we discarded results for samples whose sampling orientation or location within the core sections could not be confirmed. Outlier samples were identified following removal of low quality data, low inclination samples, and those with questionable sampling orientation or location.

3.1.1. Rock magnetism

Selected samples were chosen to study the magnetic mineralogy and identify the carriers of the NRM. Hysteresis loops were measured with fields up to ± 1.0 T, field increase of 1.5 mT, with averaging time of 150 ms per point. Acquisition of Isothermal Remanent Magnetization (IRM) was performed up to a saturation field of 2.0 T, with 100 acquisition steps and 150 ms averaging time per step. Hysteresis loops and IRM acquisition were measured using a Vibrating Sample Magnetometer (VSM) MicroMag 3900 Princeton-LakeShore Cryotronics at the Centro Oceanográfico de Registros Estratigráfico (CORE) of Instituto Oceanográfico (IO) da USP (Brazil). IRM curves were separated into discrete coercivity components using Cumulative-Log Gaussian (CLG) functions (Robertson and France, 1994) using the spreadsheet of Kruiver et al. (2001).

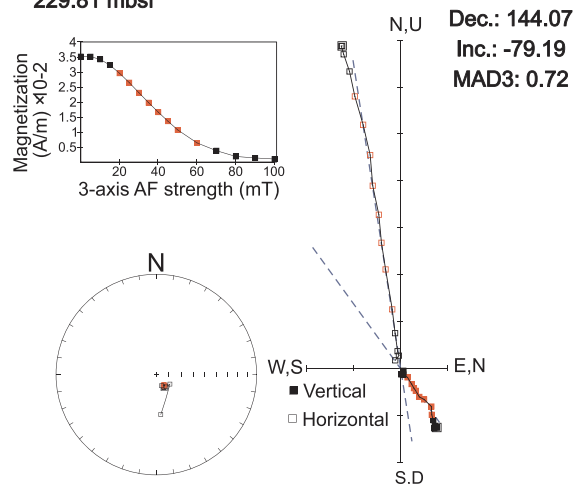
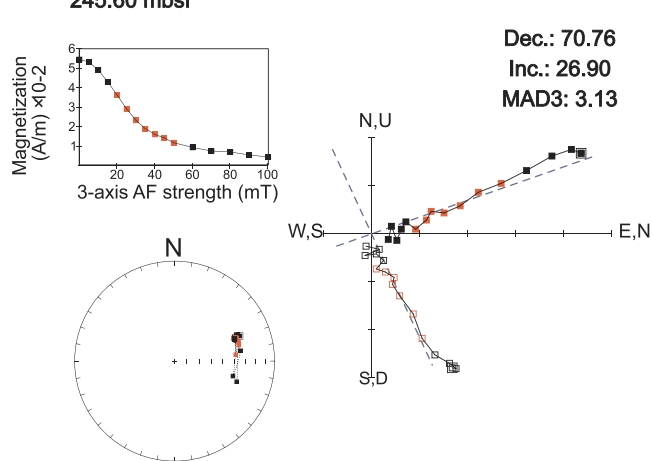
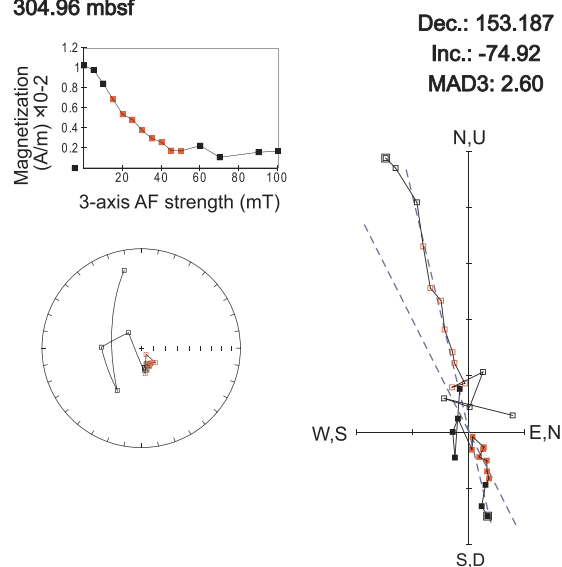
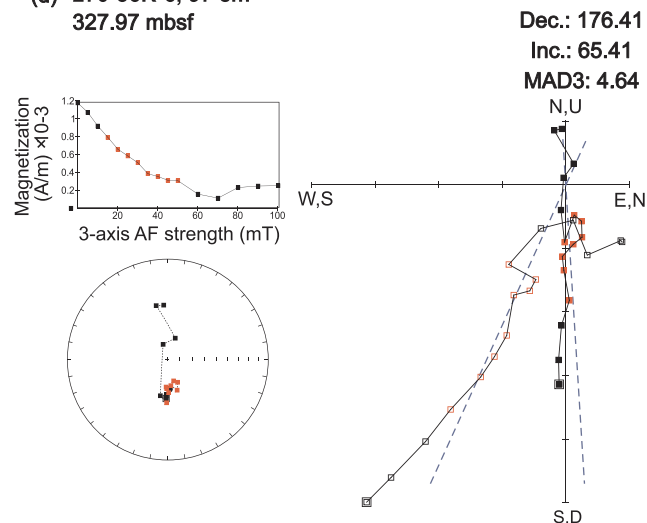
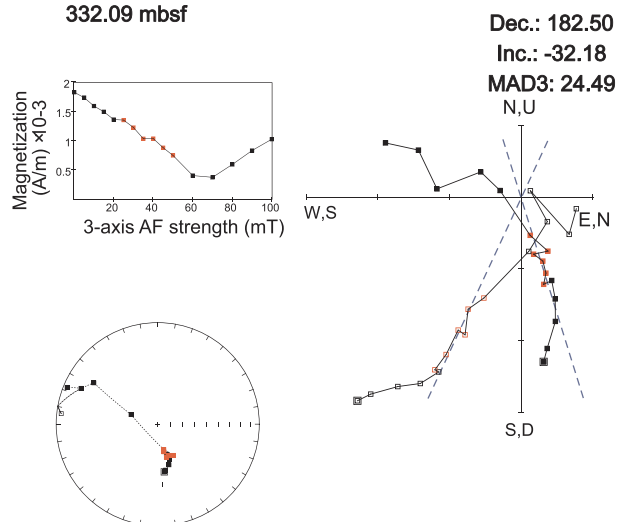
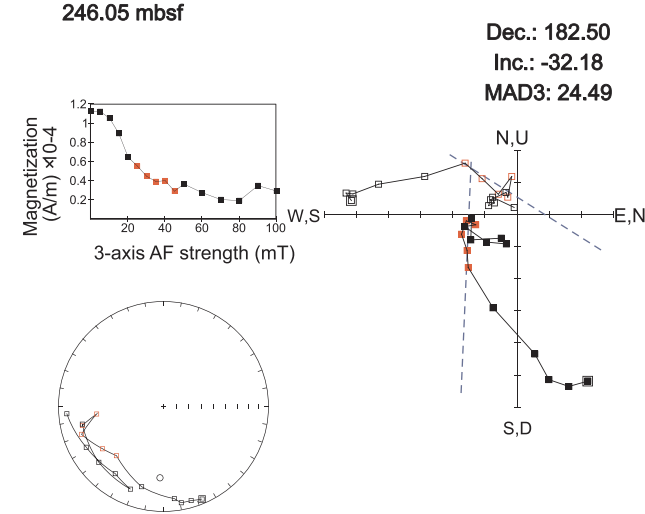
The susceptibility dependence on temperature was measured on the same samples at CORE IO-USP using a MFK1-FA Kappabridge coupled with a CS-4 furnace. The susceptibility was measured from room temperature up to 700 °C and then again during cooling back to room temperature. The measurements were performed in an inert argon atmosphere to avoid oxidation of the material with heating. The Curie (Néel) temperature of the mineralogical phases was calculated using the two-tangent method (Grommé et al., 1969).

3.2. Palynomorphs

Palynological samples were processed in the GNS Science (Lower Hutt, New Zealand) palynology laboratory. Cold 33% HCl was added to ~10–15 g of dried sample to remove carbonates. Silicates were removed by immersion in unheated 40% HF for 24 h, followed by a second cold 33% HCl wash. Samples were sonicated and filtered through a 6 µm filter to remove the very fine fraction. Samples were mounted on glass coverslips using glycerin jelly.

3.3. Calcareous nannofossils

Smear slides for examination of calcareous nannofossils were made using standard techniques (Bown and Young, 1998) at GNS Science (Lower Hutt, New Zealand). Slides were prepared thicker than usual

**(a) 270-26R-4, 71 cm
229.81 mbsf****(b) 270-28R-2, 10 cm
245.60 mbsf****(c) 270-34R-3, 146 cm
304.96 mbsf****(d) 270-36R-6, 97 cm
327.97 mbsf****(e) 270-37R-3, 9 cm
332.09 mbsf****(f) 270-28R-2, 55 cm
246.05 mbsf**

(caption on next page)

Fig. 2. Orthogonal and vector component diagrams and intensity decay plots for alternating field (AF) demagnetization data for six representative samples. Open and filled squares represent projection onto the vertical plane and the horizontal plane, respectively. Blue dotted line represents the best fit line for the characteristic remanent magnetization (ChRM), red dots represent the AF demagnetization steps chosen for the PCA. (a, c) Examples of reversed polarity ChRM; (b, d) examples of normal polarity ChRM; example of a discarded sample due to evident gyro-remanence, (f) example of discarded sample due to poor quality of the data. (For interpretation of the references to colour in this figure legend, the reader is referred to the web version of this article.)

due to the sparse amount of calcareous material in the sediment. Slides were examined using cross-polarized and plane-transmitted light on an Olympus BX-53 (GNS Science, Lower Hutt, New Zealand) or Zeiss AxioPhot A-1 light microscope (Texas A&M University, USA). For each sample, all nannofossil specimens encountered in 800 fields of view (at $630\times$) were counted. Taxonomic concepts for species are those given in [Perch-Nielsen \(1985\)](#) and [Bown \(1998\)](#).

3.4. Foraminifers

Samples were prepared for examination of foraminifer assemblages at GNS Science (Lower Hutt, New Zealand). Ten to twenty-five gram of bulk sample were soaked in tap water for a few hours to disaggregate and then washed over a $63\mu\text{m}$ sieve. The remaining residue was dried in an oven at 40°C and then weighed. All residue $> 150\mu\text{m}$ was examined using a binocular microscope and all biogenic material picked onto a slide. The $< 150\mu\text{m}$ fraction was also briefly examined for biogenic material.

3.5. K-Ar dating

Two samples for glauconite dating were broken into chips with a maximum dimension of $< 10\text{mm}$ by hammer and then further disaggregated using a repetitive freeze-thaw technique to avoid artificial reduction of rock components and contamination of finer size fractions with K-bearing minerals such as K-feldspar ([Liewig et al., 1987](#)). Grain size fractions $< 2\mu\text{m}$ were separated in distilled water according to Stokes' law and the $< 0.1\mu\text{m}$ grains were obtained using a high-speed centrifuge. Mineralogy of the size fractions was determined by X-ray diffraction (XRD) on air-dried and glycolated samples using a Philips EPD 1700 instrument and Philips APD software at CSIRO in Australia.

Potassium content was determined in duplicate by atomic absorption (Varian Spectra AA 50). Two $\sim 50\text{mg}$ sample aliquots were dissolved with HF and HNO_3 . These two sample solutions were diluted to 0.3 to 1.5 ppm K for the atomic absorption analysis. Pooled error of duplicate K determination of all samples and standards is better than 2%. The K blank was measured at 0.000033% K. Due to the hygroscopic nature of clays, care was taken in the preparation of both K and Ar sample splits. For Ar analysis by noble gas spectrometry, sample splits were loaded into clean Mo foil (Goodfellow molybdenum foil, thickness 0.0125mm , purity 99.9%), weighed and subsequently preheated to 80°C overnight to remove moisture, and weighed again using a Mettler AT20 balance. The measured dry weight was used in the K–Ar age calculation. Samples were stored in a desiccator prior to loading into the Ar purification line.

Ar isotopic determinations were performed using a procedure like that described by [Bonhomme et al. \(1975\)](#). Samples were pre-heated under vacuum at 80°C for several hours to reduce the amount of atmospheric Ar adsorbed onto the mineral surfaces during sample handling. Argon was extracted from the separated mineral fractions by fusing samples within a vacuum line serviced by an on-line ^{38}Ar spike pipette. The isotopic composition of the spiked Ar was measured with a high sensitivity on-line VG3600 mass spectrometer. The ^{38}Ar spike was calibrated against standard biotite GA1550 ([McDougall and Roksandic, 1974](#)). Blanks for the extraction line and mass spectrometer were systematically determined and the mass discrimination factor was determined periodically by airshots. Approximately 15 mg of sample material was required for Argon analyses. Two international standards (2 HD-B1 [[Hess and Lippolt, 1994](#)] and 1 LP-6 [[Odin et al., 1982](#)]) and

two airshots were also analyzed (Table S1). The error for Argon analyses is below 1.0% and the average $^{40}\text{Ar}/^{36}\text{Ar}$ value of the airshots yielded 296.02 ± 0.44 . The K–Ar ages were calculated using ^{40}K abundance and decay constants recommended by [Steiger and Jäger \(1977\)](#). The age uncertainties take into account the errors during sample weighing, $^{38}\text{Ar}/^{36}\text{Ar}$ and $^{40}\text{Ar}/^{38}\text{Ar}$ measurements, and K analysis. K–Ar age errors are within 2 sigma.

3.6. Sr isotope stratigraphy

Biogenic carbonate including shell fragments and planktonic and benthic foraminifers were selected for Sr isotope analysis based on visual inspection. Samples were dissolved in $100\mu\text{L}$ 8 M ultrapure HNO_3 loaded directly onto separation columns containing $125\mu\text{L}$ of Eichrom's Sr resin, washed with 2 mL of 8 M HNO_3 , and then collected in 1 mL 0.005 M HNO_3 . A measured blank using this method (22 pg Sr) constitutes $< 0.1\%$ of the sample loaded.

Isotopes were analyzed with a Neptune Plus multicollector inductively coupled plasma mass spectrometer (MC-ICPMS) at the University of South Carolina following methods outlined in [Scher et al. \(2014\)](#). Instrumental mass fractionation was corrected by normalizing to $^{86}\text{Sr}/^{88}\text{Sr} = 0.1194$ using an exponential law. Replicate analysis of SRM 987 yielded 0.710302 ± 0.000006 (2σ , $n = 4$) for a first set of samples, and 0.710331 ± 0.000004 (2σ , $n = 5$) for a second set. $^{87}\text{Sr}/^{86}\text{Sr}$ data were normalized to SRM 987, which has a reported $^{87}\text{Sr}/^{86}\text{Sr}$ value of 0.710248 ([McArthur, 1994](#)). Sr isotope values were converted to age estimates using the Strontium Isotope Stratigraphy Look-Up Table Version 5: Fit 26 03 13 ([McArthur et al., 2012](#)). Error estimates for the Sr ages are based on the internal error of the measurement on the mass spectrometer and the minimum and maximum age estimates from [McArthur et al. \(2012\)](#).

3.6.1. Trace element analysis

To identify postdepositional alteration of the samples which could alter the original $^{87}\text{Sr}/^{86}\text{Sr}$ value, trace- and minor-element (Mg, Na, Fe, Mn, and Ba) to calcium ratios were measured on the wash solutions of the samples immediately after loading the sample on the column, when all elements except Sr are eluted through the columns. Analysis was done on an inductively coupled plasma optical emission spectrometer (ICP-OES) at the University of Texas Arlington in the Shimadzu Center for Environmental Forensics and Material Science. Standards were prepared from Ricca or Spex brand pure, plasma-grade solutions (single and multi-element standards). Error in the ratios calculated is estimated to be better than 3% for Mg/Ca, Fe/Ca, and Mg/Ca and approximately 10% for Ba/Ca and Na/Ca based on propagated error calculated from either the average RSD calculated during analysis or analysis of a standard within the run, whichever was larger.

4. Results

4.1. Paleomagnetism

We measured the NRM of 315 samples. Examination of the ChRM components calculated using PCA show that many of the samples retain two components. The first (isolated up to 15 mT of demagnetization field) is present in most of the samples with a relatively shallow inclination that we interpret as a viscous remagnetization. The second, which is recognizable in most samples only up to 70 mT, is interpreted as the ChRM ([Fig. 2](#)). Of the 315 samples measured, 196 (62.2%) were

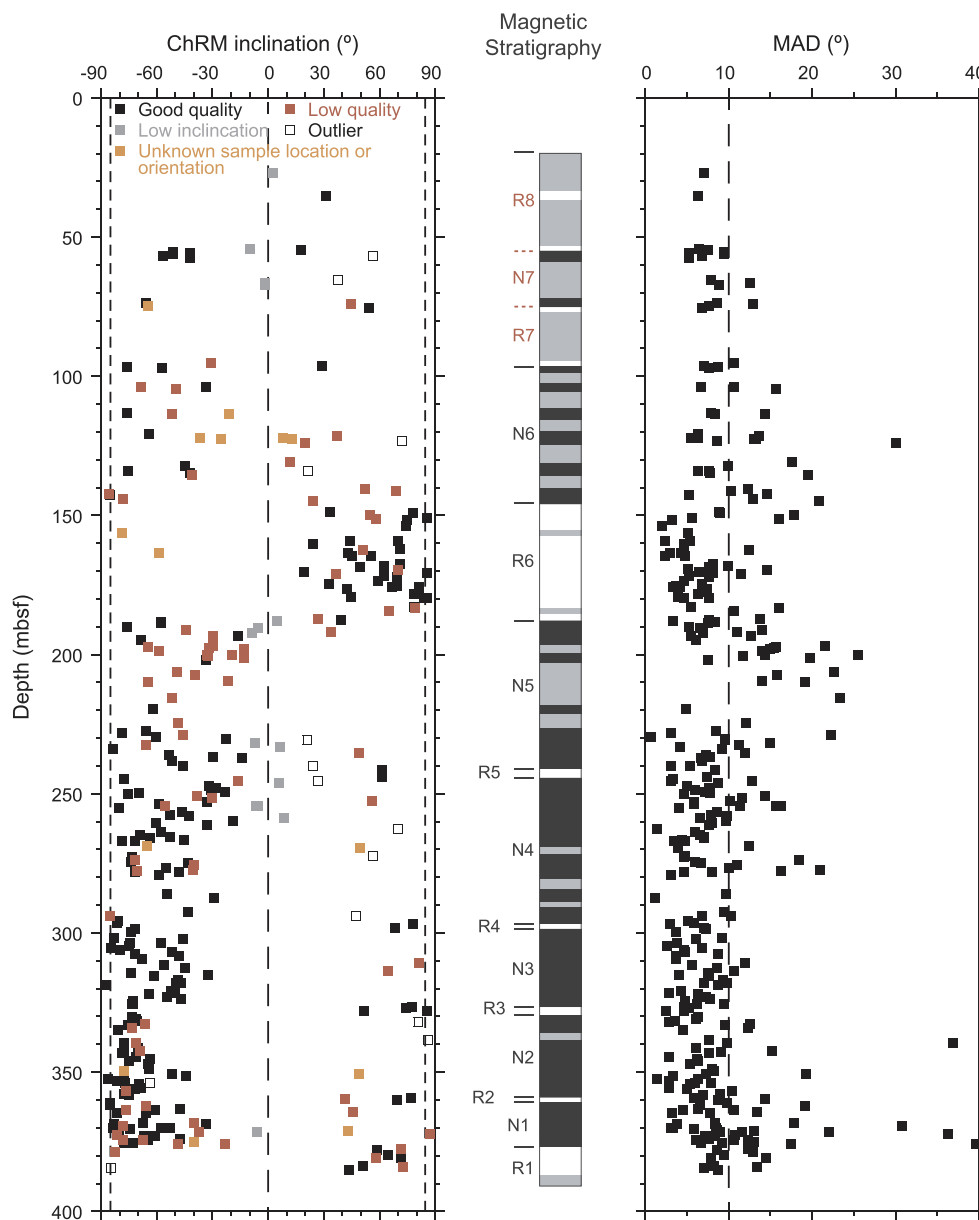


Fig. 3. Left panel: Inclination values of the ChRM versus depth. Samples are marked as “good quality”, “low quality”, “low inclination”, “outlier”, or “unknown sample location or orientation” according to the description in the text, dotted lines represent the expected GAD inclination ($\pm 84^\circ$) for the latitude of the site. Middle panel: magnetic stratigraphy and interpreted magnetozones. Red magnetozones are tentative and based on only a few samples (due to poor core recovery) that yielded inclinations shallower than expected. Right panel: MAD angle versus depth, the dotted line represent the cut-off for the differentiation between “good quality” and “low quality” data. (For interpretation of the references to colour in this figure legend, the reader is referred to the web version of this article.)

used to define magnetozones, whereas the other 119 were discarded according to the definitions given in Subsection 3.1 (Fig. 3).

Mean inclinations were calculated separately for normal and reverse polarity populations following the procedure given in Jovane et al. (2008) and are given in Table S2. A total of 52 (26.5%) samples have positive inclinations, with a mean inclination of 60.72° , whereas 144 (73.5%) show negative inclination, with a mean of -61.72° . The ChRM inclinations have a clear bimodal distribution, confirming the presence of two stable polarities (Fig. S1). It is important to remember that the original azimuthal orientation of the samples is unknown, as the cores were collected by rotary coring, which allows segments of sediment to rotate during the coring process. Therefore, the in-situ declination is unknown.

The expected geocentric axial dipole (GAD) inclination for the site latitude is $\pm 83.4^\circ$, $\sim 20^\circ$ higher than the mean inclination values of the ChRM of our samples. This result could be related to two main mechanisms: (i) inclination shallowing during deposition and diagenesis and (ii) remagnetization. Inclination shallowing is known to affect the magnetic directions in sediments and sedimentary rocks, especially in sediments that are not bioturbated (Verosub, 1977). Also, compaction

due to lithostatic load can flatten the magnetic inclinations (Anson and Kodama, 1987; Tauxe et al., 2006; Mitra and Tauxe, 2009; Li et al., 2014). In this case, the inclinations should be shallower at the base of a stratigraphic sequence and steeper towards the top, but in our case the mean inclination calculated for each magnetozone shows the opposite trend (Fig. S2), where the inclinations are shallower towards the top. Given the expected steep inclination for the stable geomagnetic field for Antarctica throughout the Cenozoic, remagnetization would have had to occurred during a short excursion or transition interval, making it also an unlikely explanation for the shallow directions. Above 100 mbsf, poor core recovery resulted in only a few samples that yielded good quality data, although with average inclinations shallower than expected and shallower than samples deeper than 100 mbsf. We have less confidence in the quality of these data points and tentatively identify magnetozones through this section of the cores.

In this study we define magnetozones as intervals where at least two consecutive samples show polarities different from adjacent intervals. The magnetic polarity record of the studied section is divided into 15 magnetozones (3 of these are tentative) that include an alternation of 8 reverse polarity (R) and 7 normal polarity intervals (N). The

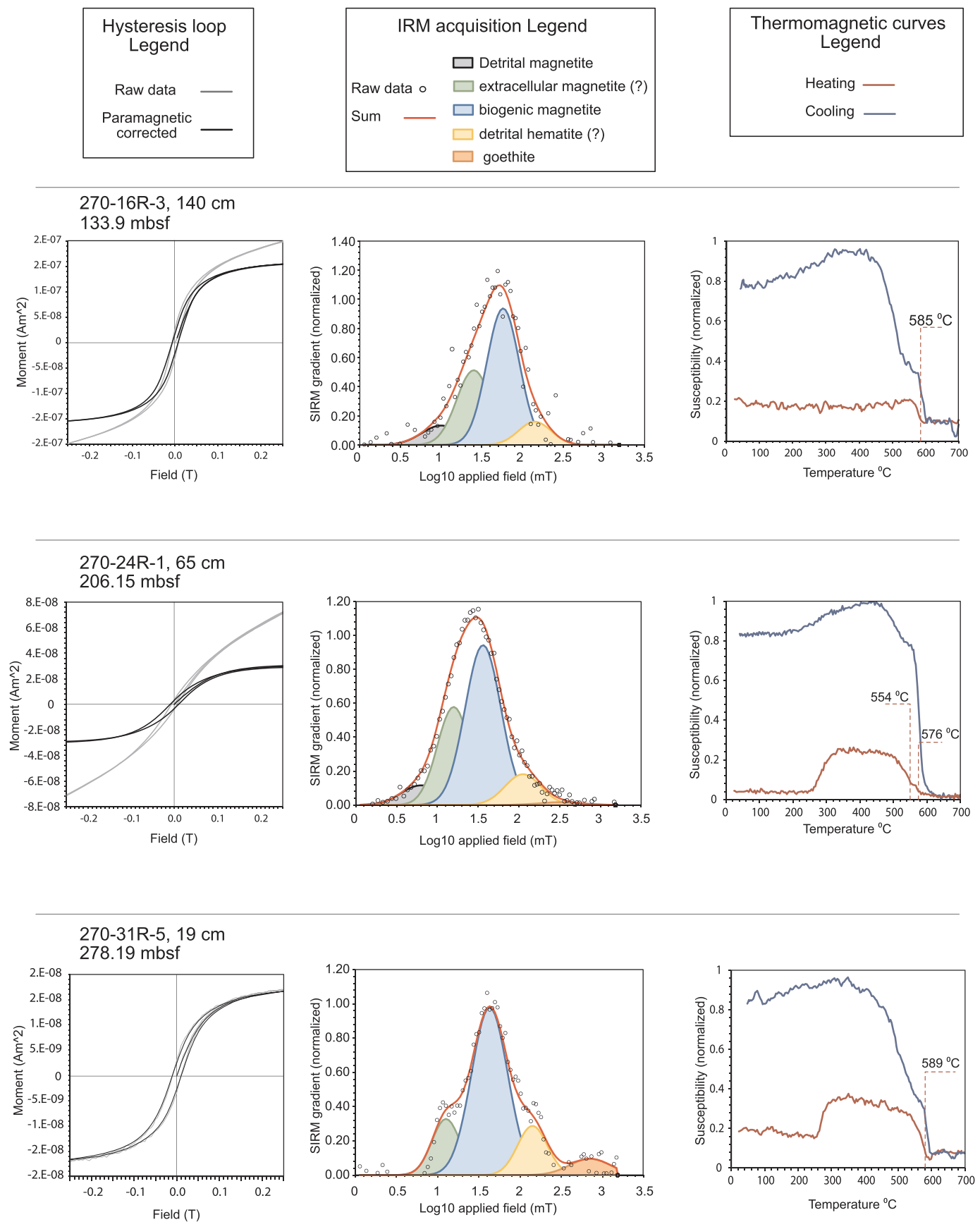


Fig. 4. Rock magnetic properties of three selected samples. It includes a hysteresis loop, the logarithmic gradient of the IRM acquisition curve separated into discrete coercivity components, and the thermomagnetic curve (susceptibility versus temperature). The Curie temperatures indicated in the graph were calculated with the two-tangent method of Grommé et al. (1969).

positions of the magnetozone boundaries are reported in Table S3. The lower limit of R1 and the upper limit of R8 correspond to the bottom and top of the studied section, respectively.

Comparison of the magnetozone recognized here and those described in the initial report (Allis et al., 1975) show some clear differences, especially in the lower half of the section, where we recognize 4 short reversal intervals that are not present in the initial report, which indicates a continuous normal polarity interval. In the upper part of the section, the position of the magnetozone is different, with the magnetozone from the shipboard report shifted some meters upward.

4.1.1. Rock magnetism

Three representative samples were selected to perform rock magnetic studies and to identify the principal magnetic carriers of the ChRM (Fig. 4). One sample was selected among those defined as “good quality” (133.90 mbsf), one classified as “low quality” (206.15 mbsf), and one that showed a clear gyro-remanence during the AF demagnetization process (278.19 mbsf). Hysteresis loops show the presence of paramagnetic minerals in all samples before paramagnetic correction, with the lowest concentration in the sample at 278.19 mbsf.

CLG decomposition of IRM acquisition curves shows the mixture of different magnetic mineral populations. The most abundant component is always represented by a mineralogical phase with a mean coercivity of 36–52 mT, and a low dispersion of 0.2. This component contributes to > 52% of the overall magnetic moment. The values of the parameters of this component are comparable to those of biogenic magnetite (Kruiver and Passier, 2001; Egli, 2004a; Jovane et al., 2012; Roberts et al., 2012). A very low coercivity component (up to 10 mT) with high dispersion (0.24) contributes to < 10%, and is interpreted as superparamagnetic (SP) detrital magnetite (Heslop et al., 2004). An intermediate component with coercivities between 13 and 25 mT and relatively low dispersion (< 0.22) comprises up to 30% of the magnetic signal, and can be interpreted as a second phase of detrital magnetite, or, alternatively, extracellular biogenic magnetite (Weiss et al., 2004;

Egli, 2004b).

High coercivity components are present in all samples. A component with a coercivity range of 120–140 mT and dispersion of 0.2–0.24 is interpreted as (possibly detrital) hematite (Kruiver and Passier, 2001), and contributes to < 15%. A second high coercivity component is present only in the sample at 278.19 mbsf. The mean coercivity of 707 mT and the fact that this component did not reach saturation in a field of 2.0 T suggest that it represents coarse hematite (Jovane et al., 2011).

Thermomagnetic curves for the sample at 133.90 mbsf show a distinct drop in susceptibility at 585 °C, which is typical of stoichiometric magnetite (Thompson and Oldfield, 1986). Samples at 206.15 and 278.19 show an increase in susceptibility values starting from ~270 °C, which can be interpreted as a mixture of the iron sulfide mineral greigite and/or titanomagnetite and maghemite. Select thermomagnetic curves for calculation of these Curie temperatures are illustrated in Fig. S3.

Given these results, we interpret that the main magnetic carrier of the ChRM is magnetite. The gyro-remanence observed in some samples is possibly linked to the field-dependent anisotropy of greigite particles (Stephenson, 1980; Robert and Weaver, 2005).

4.2. Paleontology and biostratigraphy

4.2.1. Palynomorphs

A total of 13 samples were examined for the overall palynomorph assemblage, with an initial total palynomorph census count to 300 specimens that included pollen, dinoflagellate cysts, and acritarchs (Table S4). An average of > 250 specimens were counted per slide, but fewer than 30 specimens were observed in samples 24R-3, 139–141 cm [209.89 mbsf] and 33R-3, 42–44 cm [294.42 mbsf]. Palynomorphs are present in all samples examined; acritarchs are most abundant below 200 mbsf, whereas dinoflagellates and pollen are relatively rare. Dinoflagellate abundance is highest between 180 and 120 mbsf, and

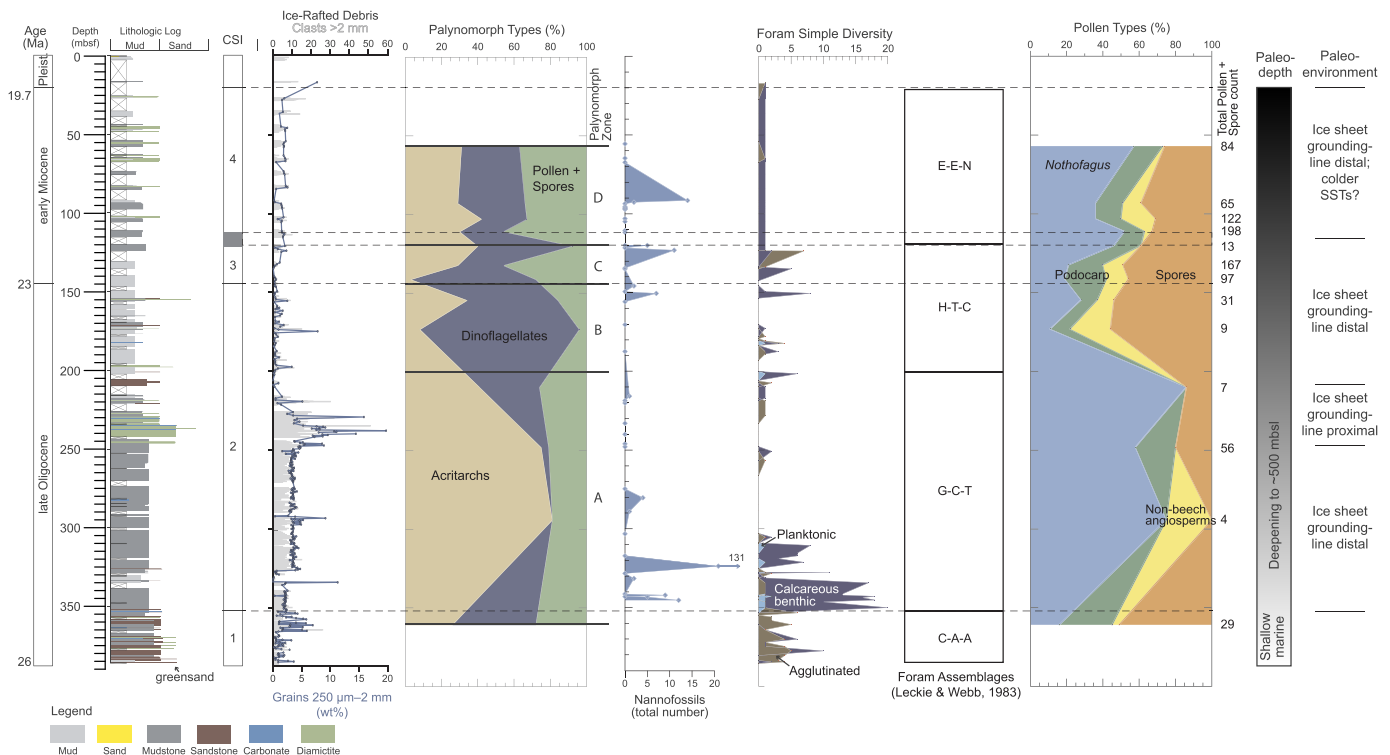


Fig. 5. Summary of lithology and ice-rafted debris (IRD) clast counts (from Kraus, 2016), distribution of palynomorph types (acritarchs, dinoflagellates, and pollen + spores), total numbers of calcareous nannofossil specimens, foraminifer simple diversity, foraminifer assemblage zones (from Leckie and Webb, 1983), distribution of pollen types, and paleoenvironmental interpretation, DSDP Site 270. CSI = chronostratigraphic interval. SST = sea-surface temperature.

pollen abundances are highest above 150 mbsf (Fig. 5).

4.2.1.1. Pollen

Pollen concentration is low throughout the section examined at DSDP Site 270, with an average of 1–2 grains/g below 150 mbsf and 8–10 grains/g above 150 mbsf (Table S4). Although these concentrations are low, they are comparable or higher than concentrations in upper Oligocene deposits in the Cape Roberts Project cores (1.5 grains/g, Prebble et al., 2006). The pollen assemblages consist of four main groups: *Nothofagidites* (southern beech), all other angiosperms, podocarps, and spores. Below 150 mbsf, pollen specimens are rare. Spores and podocarps are the most dominant components of the pollen assemblage between 125 and 150 mbsf, whereas *Nothofagidites* is more dominant above 125 mbsf (Fig. 5).

A single biostratigraphically significant pollen taxon was found in the Site 270 samples. Seven specimens of *Tricolpites* sp. a (sensu Askin and Raine, 2000) were found between 141.4 and 93.22 mbsf (Table S4; Fig. 6). This species is a latest Oligocene (first appearance in Chron C6C) marker taxon in the Ross Sea region (Askin and Raine, 2000; Wilson et al., 2000; Prebble et al., 2006). Samples below 141.4 mbsf have sparse spore-pollen assemblages; however, this species was not found in any of the samples examined below that depth.

4.2.1.2. Dinoflagellates

An additional 14 samples were examined for dinoflagellate cysts (Table S5). Two samples from below 386 mbsf were barren of dinoflagellates. The remaining samples contain species-poor assemblages consisting primarily of *Lejeunecysta* and *Selenopemphix*, which occur in all of the productive samples to the top of the sequence. Less common *Batiacasphaera*, *Operculodinium*, and a few other genera appear sporadically, typically in only one or a few samples (Table S5; Fig. 7). These exhibit a very slight trend for increased diversity towards the top of the sequence.

Eight age-diagnostic taxa are present throughout the section and allow assignment to dinoflagellate zones defined at the relatively nearby Cape Roberts Project drill site (Clowes et al., 2016) (Table S5). We also attempted to reconcile the Site 270 assemblages with the Integrated Ocean Drilling Program (IODP) Hole U1356A (Wilkes Land) zonation of Bijl et al. (2018) but abandoned this effort due to several difficulties. These include a lack of key indicator species in common between the two locations (for example, *Lejeunecysta striata* is the most common taxon at Site 270, but is either absent or was not identified in Hole U1356A), and apparent diachronism of the important *Lejeunecysta acuminata* last appearance datum (LAD). This comparison should be a priority for future study, paying particular attention to the form identified herein as *Lejeunecysta* cf. *attenuata*, which occurs in Site 270 and Hole U1356A but not at Cape Roberts.

The sample from 384.67 mbsf contains *L. acuminata* and *Lejeunecysta rotunda*, which are characteristic of the Oligocene and allow assignment of this sample to the *Lejeunecysta katatonos*-*Cymatiosphaera robertsii*

Zone. Samples between 383.44 and 383.60 mbsf contain *L. cf. attenuata*, suggesting an Oligocene age and allowing tentative assignment of these samples to the *C. robertsii* Zone. The sample from 350.22 mbsf contains *L. acuminata* and *L. striata*. These two species have not been reported occurring together at Cape Roberts and their co-occurrence here is tentatively thought to be indicative of an Oligocene to Miocene age (*Cymatiosphaera* cf. *invaginata*-*L. striata* Zones). Between 150.50 and 343.00 mbsf, the only age diagnostic taxon present is *L. striata*, indicating the *L. striata* Zone and an Oligocene–Miocene age. Samples above 93.20 mbsf also contain *Batiacasphaera cooperi*, which indicates a Miocene age within Chron C6An.2n (< 20.7 Ma) (Florindo et al., 2005; Clowes et al., 2016). The continued presence of *L. striata* allows assignment of samples between 93.20 and 27.26 mbsf to the *L. striata* Zone.

4.2.2. Calcareous nannofossils

A total of 46 samples were examined for calcareous nannofossils. Of these, only 14 samples contain nannofossils (Table S6). In most of these samples, calcareous nannofossils are extremely rare, with < 20 specimens encountered within 800 fields of view. One sample, from 327.76 mbsf, contains greater numbers of nannofossil specimens (approximately 1 specimen per 6 fields of view). The nannofossil assemblage primarily consists of reticulofenestrids, including members of the genera *Cyclicargolithus*, *Dictyococcites*, and *Reticulofenestera* (Fig. 8). Extremely rare specimens of *Chiasmolithus altus* and *Zygrhablithus bijugatus* were also encountered. In addition to the nannofossils, a few specimens of calcispheres (calcareous dinoflagellates) are also present.

The assemblage includes three biostratigraphically significant taxa: *C. altus*, *Z. bijugatus*, and *Dictyococcites bisectus* (Table S6). A single specimen of *C. altus* was found at 345.29 mbsf, which corresponds to the deepest sample examined. The highest occurrence (HO) of *Z. bijugatus* is assigned to the sample from 280.25 mbsf based on a single specimen. The HO of *D. bisectus* is identified at 150.65 mbsf. This sample contained four specimens of this taxon, and this species is also consistently present in samples containing calcareous nannofossils below this depth. We note that these biostratigraphically significant events are highest occurrences and therefore could be reworked in the section. Therefore, they represent a maximum age at the horizons to which they are assigned.

4.2.3. Foraminifers

A total of 95 samples were examined for foraminifers (Table S7). Of these, 45 contained either no foraminiferal material or poorly preserved remnants of foraminifers, rendering them unidentifiable. The remaining 50 samples contained identifiable foraminifer specimens. Planktonic foraminifers are extremely rare in the examined samples. A single globigerinoid specimen was found in sample 23R-4, 110–112 cm (201.60 mbsf) and a possible specimen of *Globigerinoides trilobus* was found in sample 38R-4, 0–4 cm (343.00 mbsf). Two additional foraminifer specimens may be planktonic foraminifers, but may not

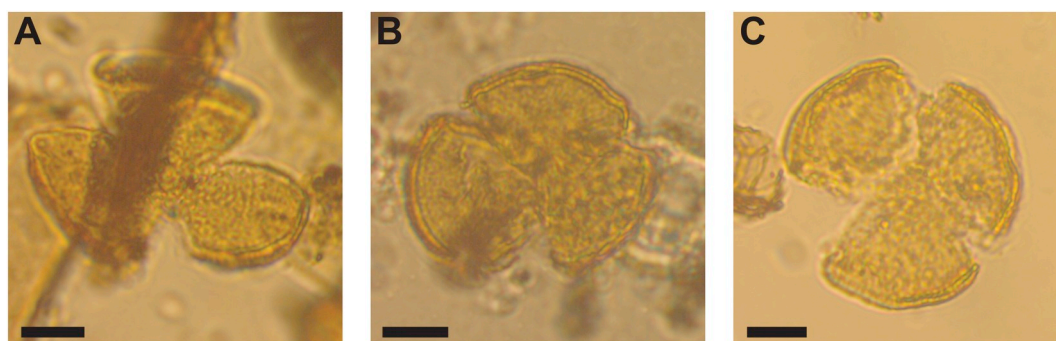


Fig. 6. Photomicrographs of *Tricolpites* sp. a (sensu Askin and Raine, 2000). Scale bar is 10 μm in all images. (A) 270-8R-3, 64–68 cm; specimen is 45 μm in diameter. (B) 270-14R-1, 61–63 cm; specimen is 39 μm in diameter. (C) 270-17R-2, 88–90 cm; specimen is 40 μm in diameter.

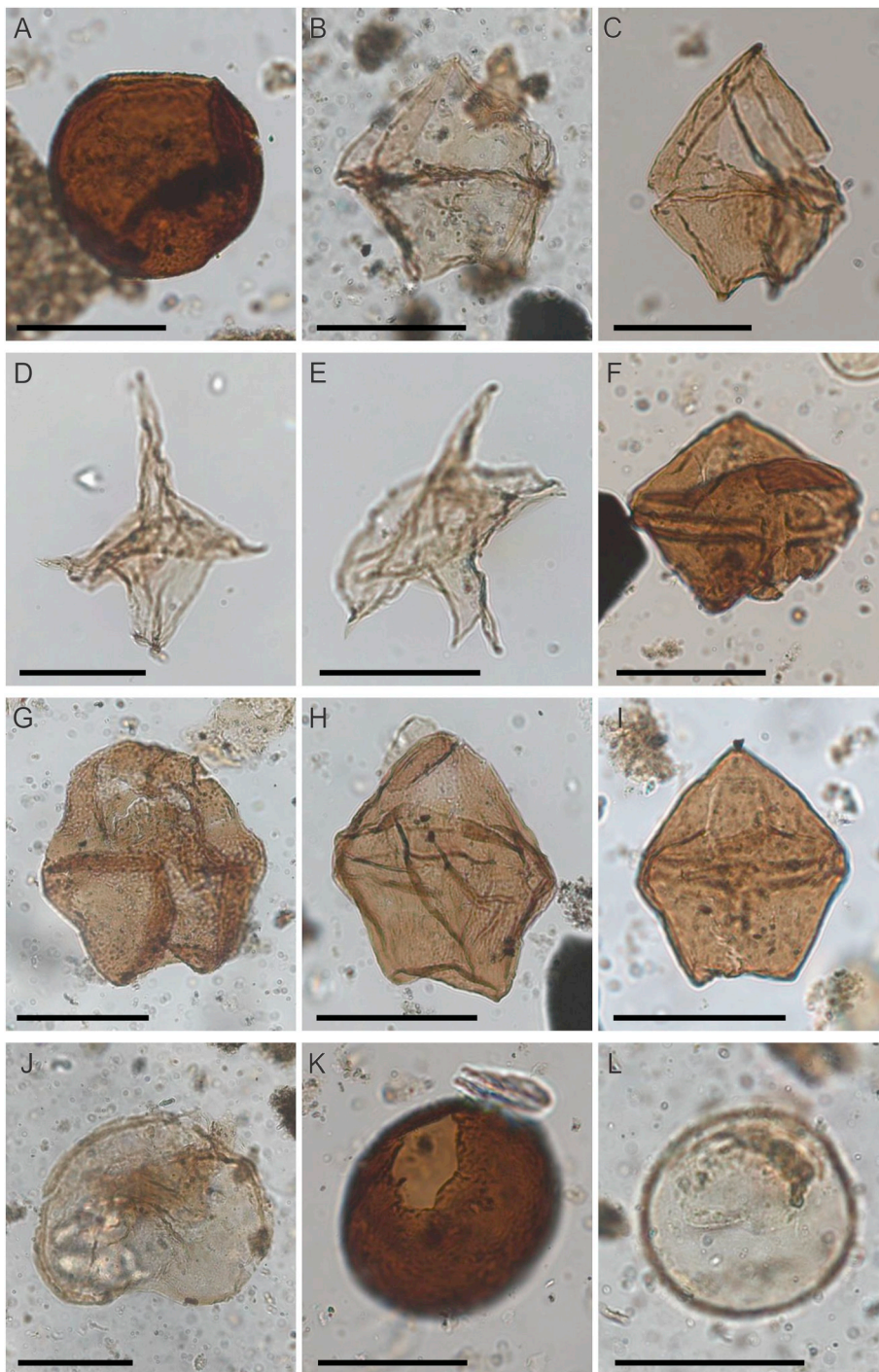


Fig. 7. Photomicrographs of dinoflagellates. Scale bar is 50 μm in all images. (A) *Brigantidium pynei*? (270-8R-3, 64–68 cm; 68 \times 70 μm). (B) *Lejeunecysta fallax* (270-43R-5, 93–103 cm; 77 \times 74 μm). (C) *Lejeunecysta acuminata* (270-15R-1, 19–22 cm; 76 \times 71 μm). D–E. *Lejeunecysta* cf. *attenuata* (270-43R-5, 93–103 cm; D. 112 \times 90 μm ; E. 72 \times 71 μm). (F) *Lejeunecysta katatonos* (270-5R-2, 26–31 cm; 65 \times 76 μm). (G) *Lejeunecysta rotunda* (270-43R-6, 67–69 cm; 91 \times 86 μm). (H) *Lejeunecysta striata* (270-18R-2, 50–54 cm; 82 \times 70 μm). (I) *Lejeunecysta* cf. *striata* (270-8R-3, 64–68 cm; 70 \times 62 μm). (J) *Selenopemphix nephroides* (270-43R-5, 93–103 cm; 80 \times 101 μm). (K) *Batiacasphaera cooperi* (270-13R-2, 49–60 cm; 75 \times 73 μm). (L) *Malvinia* cf. *escutiana* (270-43R-5, 93–103 cm; 55 \times 56 μm).

represent the in-situ assemblage and may instead be reworked.

Benthic foraminifers were more abundant in the examined assemblages (Table S7). *Antarcticella antarctica* (originally considered a planktonic, but now known to be a benthic foraminifer [Liu et al., 1998]) was found in 12 of the examined samples. *Candeina zealandica* is also found in some of the examined samples. There are a few key paleodepth indicators, although the fauna in general appears to represent shelf paleodepths. In the upper part of the hole, *Cyclammina rotundata* is recorded in samples 15R-3, 72–75 cm (123.72 mbsf) and 21R-4, 80–83.5 cm (182.30 mbsf). Hayward (1986) reports *C. rotundata* at middle to abyssal paleodepths for the lower Miocene of New Zealand. *Cibicides temperata*, found in sample 15R-3, 48–51.5 cm (123.48 mbsf) and moderately common in the lower section, is reported by Hayward

(1986) as mainly mid- to outer shelf but also ranging down to middle bathyal. *Cibicides pseudoungeriana* and *Cibicides mediocris* are sparsely present through the site. van Morkhoven et al. (1986) synonymize *C. pseudoungeriana* and *C. mediocris* with *Cibicides pachyderma*, which is considered primarily an upper bathyal dweller.

The lower part of the hole has more bathyal indicators. *Cyclammina incisa* is recorded as middle shelf to abyssal by Hayward (1986). *Cibicides mediocris* is also present and *Cibicides temperata* is relatively common. *Melonis barleeianum* is considered a shelf to bathyal dweller by Holbourn et al. (2013). *Pullenia bulloides* is recorded by Crundwell et al. (1994) as upper bathyal or deeper and *Oridorsalis tenera* is also considered a bathyal species. A single specimen of *Cibicides robertsonianus* was recorded in sample 38R-5, 79–83 cm (345.29 mbsf). Holbourn et al.

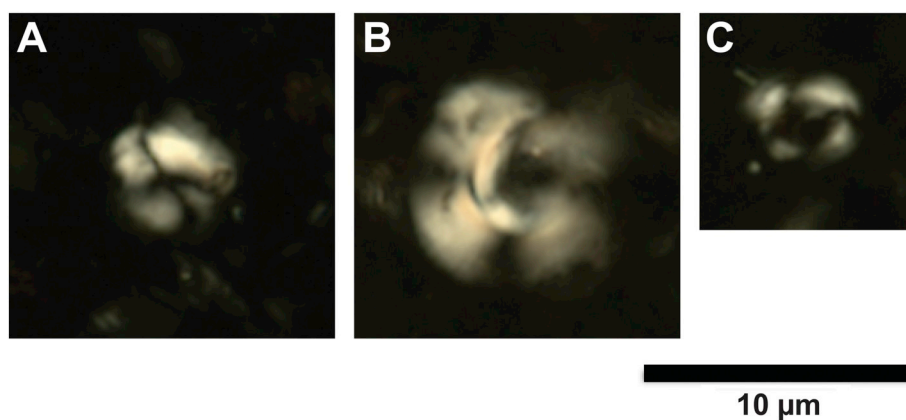


Fig. 8. Photomicrographs of calcareous nannofossils. (A) Broken specimen of *Dictyococcites bisectus* (270-36R-6, 76–80 cm). (B) *Cyclocargolithus floridanus* (270-25R-1, 85–87 cm). (C) *Reticulofenestra hampdenensis* (270-32R-CC).

(2013) and van Morkhoven et al. (1986) consider *C. robertsonianus* a bathyal to abyssal dweller. Data from GNS Science files place it at middle bathyal or deeper in New Zealand.

Despite few bathyal restricted species there is enough evidence to place the location of Site 270 at bathyal depths (> 200 m), at least from 123.72 mbsf (15R-3, 72–75 cm) down to 385 mbsf (just above the glauconitic sandstone), and it may have been as deep as middle bathyal (600–1000 m).

4.3. Glauconite K–Ar ages

Two samples of glauconitic sandstone from 385.09 and 385.24 mbsf were dated using the K–Ar method (Table S8). Glauconite from the $< 2\mu\text{m}$ size fraction of both samples yielded ages of $32.9\text{ Ma} \pm 1.2\text{ m.y.}$ and $33.6\text{ Ma} \pm 1.2\text{ m.y.}$, respectively. However, these samples both contain clay impurities that may be reworked from older rocks and therefore yield older ages.

We also measured the K–Ar of the $< 0.1\mu\text{m}$ fraction of the sample from 385.09 mbsf, which yielded an age of $25.9\text{ Ma} \pm 1.5\text{ m.y.}$ This age agrees with previous K–Ar results, which yielded an age of $26.1\text{ Ma} \pm 0.4\text{ m.y.}$ for the sample with the least amount of clay impurities (McDougall, 1977).

4.4. Sr isotopes and trace elements

Ten samples yielded Sr-isotope ages ranging from $23.0\text{ Ma} \pm 0.30\text{ m.y.}$ to $27.03\text{ Ma} \pm 0.47\text{ m.y.}$ (Table S9), which is consistent with the expected age of the section based on biostratigraphy and K–Ar dating. However, the ages do not increase progressively downhole and instead show significant scatter. Trace element analysis shows high Mg/Ca values $> 10\text{ mmol/mol}$ (Table S9) indicating recrystallization and/or incorporation of Mn–Fe oxyhydroxides of MnCO_3 coatings.

5. Discussion

5.1. Age model

The age model for DSDP Site 270 utilizes biostratigraphy, $^{87}\text{Sr}/^{86}\text{Sr}$ dating of macro- and microfossils, magnetostratigraphy, and K–Ar dating of glauconite to correlate rock units to the Global Polarity Timescale (GPTS) (Ogg, 2012). Key events and tie points are summarized in Table 1. Biostratigraphic datums include first (lowest) and last (highest) appearances of dinoflagellate cysts, calcareous nannofossils, diatoms, pollen, and foraminifers. Ages for these datums are primarily derived from published literature. We present three alternate age-depth models that are defined by distinct lines of correlation (LOC) to the

GPTS (Fig. 9). Our preferred model is described in detail below.

We divided the stratigraphic interval from 386 to 20 mbsf in DSDP Site 270 into four chronostratigraphic intervals (CSIs), which are separated by disconformities.

5.1.1. CSI 1 (389 to 352 mbsf)

The lowermost 34 m of the section examined contains a 1 m-thick glauconite-rich fine sandstone unit that is overlain by a thick sequence of decimeter-scale sandstone and mudstone interbeds. Petrographic examination of the glauconitic sandstone unit revealed well-preserved glauconite grains that show little sign of alteration. Importantly, glaucony forms during deposition of sediment at the water/sediment interface and offers an attractive target to isotopically date the time of glauconitic sandstone deposition. A sample from the interval 385.09–385.11 mbsf was prepared for K–Ar analysis and radiometric ages of $25.9\text{ Ma} \pm 1.6\text{ m.y.}$ and $32.9\text{ Ma} \pm 1.2\text{ m.y.}$ were determined for the $< 0.1\mu\text{m}$ and $< 2\mu\text{m}$ size fractions, respectively. Whereas we cannot exclude the possibility that the glauconitic sandstone is lowermost Oligocene, impurities likely influence the dates derived from the $< 2\mu\text{m}$ fraction. Therefore, we favor the younger age ($25.9 \pm 1.6\text{ Ma}$) derived from the $< 0.1\mu\text{m}$ fraction. The HO of *Lejeunecysta rotunda* (D5; 24.5 Ma) at 383.84 mbsf supports this inference. We also note that this age is consistent with that derived for the glauconitic sandstone unit in a previous study (McDougall, 1977). The age of sediments between 384 and 350 mbsf is difficult to constrain due to the paucity of age diagnostic events within the 34 m-thick interval. The absence of *L. rotunda* in samples above 383 mbsf is most likely due to environmental factors, as foraminifers (Leckie and Webb, 1983), lithofacies analysis, and seismic data (De Santis et al., 1995, 1999) indicate that the basin was subsiding during this interval. The age at the top of the interval is constrained by the HO of *Chiasmolithus altus* (CN3) at 345.29 mbsf. This datum indicates that sediments below this stratigraphic level must be older than 25.44 Ma. Magnetostratigraphic reversal stratigraphy is characterized by a clear reversal (MR12) at the R1/N1 boundary (between 378.06 and 375.40 mbsf) that we correlate to the C8r/C8n.2n boundary (25.987 Ma). We suggest that magnetozone R2 is likely unreliable or could represent a short duration cryptochron not defined in the geomagnetic polarity timescale.

5.1.2. CSI 2 (352 to 149–146 mbsf)

A significant change in the benthic foraminifer assemblage occurs at 352 mbsf and is inferred to indicate a chronostratigraphic break (Leckie and Webb, 1983, 1986). This assemblage change approximately coincides with a transition from sandstone and mudstone interbeds to a 100 m-thick sequence of predominantly massive mudstone containing dispersed to abundant IRD. We place a disconformity (U6) at 352 mbsf based on the foraminifer assemblage data and lithologic change to more

Table 1
List of datums/events and ages used for Site 270 age model in Fig. 6. Magnetic reversals marked with an asterisk (*) are based on only a few samples (due to poor core recovery) that yielded inclinations shallower than expected and are therefore only tentatively identified.

Sample ID	Datum label ^a	Depth (mbsf) ^b	Event ^c	Age (Ma)	Error (m.y.) ^d	Event source	Stratigraphic range/Age source	Comment ^e
270-5R-2, 26–31 cm	U1	20	Unconformity 1	> 18 Ma		This study	Clowes et al. (2016); Florindo et al. (2005)	At 79.44 mbsf in CRP-2; within Chron C5En (18.056–18.524 Ma)
	D1	27.30	HO <i>Lejaneuxysta striata</i>			This study	Gradstein et al. (2012)	
	MR1*	55.43–54.71	Reversal N7/R8 (C6An.1n/C6r)	20.04		This study		
270-8R-3, 64–68 cm	D2	57.14	HO <i>Batiacaspheara cooperi</i>	> 18 Ma		This study	Clowes et al. (2016); Florindo et al. (2005)	At 85.36 mbsf in CRP-1; within Chron C5En (18.056–18.524 Ma)
270-9R-3, 128–130 cm	S1	67.28		23.4	0.3	This study	LOWESS 5 Fit 26 03 13 (McArthur et al., 2012)	
	MR2*	75.41–73.69	Reversal R7/N7 (C6An.1r/C6An.1n)	20.213		This study	Gradstein et al. (2012)	
270-12R-2, 19.5–21.5 cm	D3	93.20	HO <i>Brigantedinium pynei</i>	< 23.295		This study	Clowes et al. (2016); Florindo et al. (2005)	At 181.74 mbsf in CRP-2A, within Chron C6Cn.3n (23.233–23.295 Ma)
	MR3*	96.85–96.33	Reversal N6/R7 (C6An.2n/C6An.1r)	20.439		This study	Gradstein et al. (2012)	
270-13R-3, 110–112 cm	D1	105.00	HO <i>Kislevella tricornata</i>	> 20.439		Steinhauff et al. (1987)	Olney et al. (2007); Florindo et al. (2005)	LCO at 120.33 mbsf in CRP-2/2A, within Chron C6An.2n (20.439–20.709 Ma)
270-12R-2, 19.5–21.5 cm	D4	93.20	LO <i>Batiacaspheara cooperi</i>	< 20.7		This study	Clowes et al. (2016); Florindo et al. (2005)	At 113.51 mbsf in CRP-2A, within Chron C6An.2n (20.439–20.709 Ma)
270-14R-2, 96–99 cm	S2	112.96		23	0.3	This study	LOWESS 5 Fit 26 03 13 (McArthur et al., 2012)	
270-17R-2, 88–90 cm	U2	121–112	Unconformity 2			This study	Askin and Raine (2000); Prebble et al. (2006); Florindo et al. (2005)	At 287 mbsf in CRP-2, within Chron C7n.2n (24.109–24.474 Ma)
	P1	141.40	LO <i>Tricolpites</i> sp. a	< 24.474		This study	Gradstein et al. (2012)	
	MR4	148.68–142.64	Reversal R6/N6 (C6Cr/C6Cn.2n)	23.03		This study		
	U3	149–146	Unconformity 3			This study	Gradstein et al. (2012)	
270-18R-2, 82.5–85.5 cm	CN1	150.65	HO <i>Dictyococites bisectus</i>	23.13		This study		
	MR5	188.38–187.72	Reversal N5/R6 (C7n.1n/C6Cr)	23.962		This study	Gradstein et al. (2012)	
270-22R-1, 45 cm	S3	187.45		25.1	0.35	This study	LOWESS 5 Fit 26 03 13 (McArthur et al., 2012)	
	U4	198	Unconformity 4			This study		
270-23R-4, 110–112 cm	S4	201.60		24.95	0.375	This study	LOWESS 5 Fit 26 03 13 (McArthur et al., 2012)	
270-25R-1, 85–87 cm	S5	215.85		24.46	0.28	This study	LOWESS 5 Fit 26 03 13 (McArthur et al., 2012)	
	MR6	241.38–240.11	Reversal R5/N5 (C7r/C7n.2n)	24.474		This study	Gradstein et al. (2012)	
	U5	246	Unconformity 5			This study		
	MR7	244.68–244.11	Reversal N4/R5 (C7An/C7r)	24.761		This study	Gradstein et al. (2012)	
	MR8	297.02–296.41	Reversal R4/N4 (C7Ar/C7An)	24.984		This study	Gradstein et al. (2012)	
	MR9	298.66–298.41	Reversal N3/R4 (C8n.1n/C7Ar)	25.099		This study	Gradstein et al. (2012)	
270-31R-6, 75 cm	CN2	280.25	HO <i>Zygrhabditus bijugatus</i>	23.76		This study	Gradstein et al. (2012)	
270-32R-5, 85–87 cm	S6	288.35		27.025	0.45	This study	LOWESS 5 Fit 26 03 13 (McArthur et al., 2012)	
270-35R-5, 70–72 cm	S7	317.20		23.37	0.23	This study	LOWESS 5 Fit 26 03 13 (McArthur et al., 2012)	
	MR10	326.73–325.50	Reversal R3/N3 (C8n.1r/C8n.1n)	25.264		This study	Gradstein et al. (2012)	

(continued on next page)

Table 1 (continued)

Sample ID	Datum label ^a	Depth (mbsf) ^b	Event ^c	Age (Ma)	Error (m.y.) ^d	Event source	Stratigraphic range/Age source	Comment ^e
270-36R-6, 76–78 cm	S8	327.76		23.5	0.275	This study	LOWESS 5 Fit 26 03 13 (McArthur et al., 2012)	
	MR11	330.29–328.22	Reversal N2/R3 (C8n.2n/C8n.1r)	25.304		This study	Gradstein et al. (2012)	
270-37R-4, 79–81 cm	S9	334.29		26.375	0.45	This study	LOWESS 5 Fit 26 03 13 (McArthur et al., 2012)	
270-38R-4, 0–4 cm	F1	343.00	LO <i>Globigerinoides trilobus</i>	22.96		This study	Gradstein et al. (2012)	
270-38R-5, 79–83 cm	CN3	345.29	HO <i>Chiasmolithus altus</i>	25.44		This study	Gradstein et al. (2012)	
270-38R-5, 79–83 cm	S10	345.29		24.55	0.28	This study	LOWESS 5 Fit 26 03 13 (McArthur et al., 2012)	
	U6	352	Unconformity 6			This study	Gradstein et al. (2012)	
	MR12	378.06–375.40	Reversal R1/N1 (C8r/C8n.2n)	25.987		This study		
270-43R-5, 93–103 cm	D5	383.84	HO <i>Lefaeucysta rotunda</i>	> 24.5		This study	Clowes et al. (2016); Florindo et al. (2005)	At 307.0 mbsf in CRP-2, in C7n.2n (24.109–24.474 Ma)
270-43R-6, 109 cm		385.09	K-Ar dating of glauconitic sandstone	25.9	1.45	This study		

^a D = dinoflagellate, MR = magnetic reversal, S = strontium isotope age, Di = diatom, P = pollen, CN = calcareous nannofossil, F = foraminifer.

^b Depth range for magnetic reversal indicates top and base depth of samples that show a magnetic polarity reversal. See Table S2.

^c HO = highest occurrence. LO = lowest occurrence.

^d Error = analytical error and minimum/maximum age estimates from McArthur et al. (2012) for Sr-isotope dating; sample weighing, Ar isotope measurements, and K analyses for K–Ar dating.

^e CRP = Cape Roberts Project, LCO = last common occurrence.

abundant IRD and designate the boundary between CSI 1 and CSI 2 at this break. We note that a regional seismic reflector (Base Glacial Marine [BGM] of P. Bart, personal communication) approximately coincides with this horizon. The HO of *Chiasmolithus altus* (CN3) at 345.29 mbsf indicates that sediments above the U6 disconformity must be 25.44 Ma in age or younger. Therefore, the maximum span of time represented in the U6 disconformity is unlikely to exceed ~500 k.y. (< MR12 [25.987 Ma] and > CN3 [25.44 Ma]). The stratigraphic record lacks information required to further constrain the break.

The top of CSI 2 is defined by disconformity U3 (149 to 146 mbsf). This horizon approximately coincides with a major seismic reflector (mid-270) that is mapped across the central and eastern Ross Sea and is interpreted to represent an episode of major erosion across the Ross Sea (C. Sorlien, personal communication). Unfortunately, sediment was not recovered through the interval from ~149 to 146 mbsf, so direct lithostratigraphic evidence of an erosional contact is unavailable. However, we note that there is an eight to 10-fold increase in pollen content between samples examined at 154.74 and 141.38 mbsf, which suggests a change in local environmental or depositional conditions across the boundary, together with a background increase in IRD abundance above 140 mbsf (Fig. 5; Kraus, 2016). Key biostratigraphic datums include the HO of *Dictyococcites bisectus* (CN1) at 150.65 mbsf, which requires that sediments above this horizon are younger than 23.13 Ma and the lowest occurrence (LO) of *Tricolpites* sp. a sensu Askin and Raine (2000) at 141.4 mbsf, which suggests that sediments below this horizon are older than 24.474 Ma based on the occurrence of this datum within Chron C7n.2n at CRP-2 (Florindo et al., 2005). These data indicate that a maximum 1.3 million years of record is missing in U3, although the time break is likely < 1 million years based on our preferred correlation (Fig. 9).

Other biostratigraphic datums within CSI 2 include the HO of *Zygrhablithus bijugatus* (CN2) at 280.25 mbsf. This occurrence is consistent with our LOC as it requires that sediments below this level are older than 23.76 Ma. This datum also indicates that sediments above this datum could be younger than 23.76 Ma; however, we suggest this is a minimum age for the sediments at this horizon and infer that the HO of this species in DSDP 270 represents a local LAD and that its stratigraphic range is incomplete due to local environmental factors. We note that the shipboard identification of *Globigerinoides trilobus* (F1) at 253 mbsf is problematic. This datum requires that the sediments above this horizon are 22.96 Ma or younger. However, Kaneps (1975) indicated that this single specimen may be a result of contamination, as the species was not known from high latitudes. Furthermore, our investigation found a possible specimen of *G. trilobus* in sample 38R-4, 0–4 cm (343 mbsf). This suggests that the specimens assigned to this taxon from Site 270 are a different species or have a different stratigraphic range than at lower latitudes. Therefore, we infer that this reported occurrence in Kaneps (1975) is unreliable.

Our preferred LOC fits ⁸⁷Sr/⁸⁶Sr dates (S3–S5) quite closely, requiring only relatively minor up-section reworking of S3 and S4. We note that this correlation model contradicts ⁸⁷Sr/⁸⁶Sr dates on foraminifer tests at 317.2, 327.76, and 345.29 mbsf (S7, S8, and S10). These datums suggest that the sediments are younger than indicated by our preferred model. A correlation model that fits the “young” ⁸⁷Sr/⁸⁶Sr ages requires that the calcareous nannofossil events CN1–CN3 are reworked up section, which is not uncommon in glaciomarine sediments. However, the correct biostratigraphic sequence of these HOs is preserved, which suggests that major up-section reworking is unlikely. Therefore, we suspect that post-depositional diagenesis may have affected the strontium dates derived from the tests.

Magnetic reversals within CSI 2 allow us to further constrain our preferred LOC. We correlate N2/R3 (MR11) with C8n.2n/C8n.1r (25.304 Ma) and R3/N3 (MR10) with C8n.1r/C8n.1n (25.264 Ma). We correlate N3/R4 (MR9) with C8n.1n/C7Ar (25.099 Ma), R4/N4 (MR8) with C7Ar/C7An (24.984 Ma), and N4/R5 (MR7) with C7An/C7r (24.761 Ma). Magnetozones R5 spans a short interval between 244.40

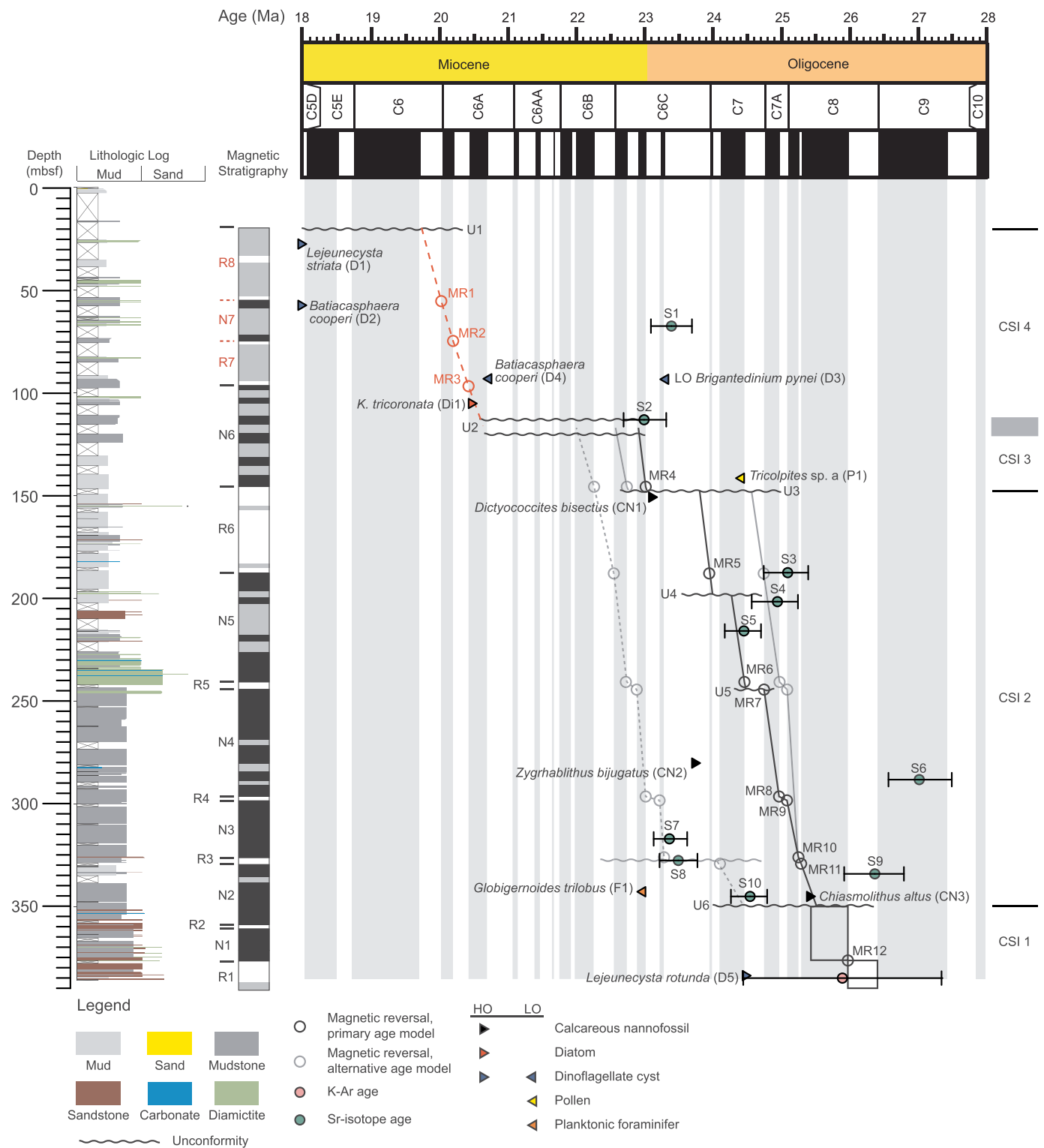


Fig. 9. Revised age-depth model for Site 270 showing our preferred line of correlation (LOC; black line) and two alternate interpretations (grey solid and dashed lines). Red magnetic reversals and dashed red LOC indicate tentative magnetostratigraphic zones based on only a few samples (due to poor core recovery) that yielded inclinations shallower than expected. We have less confidence in these data points. No LOC is given for CSI 1 due to limited chronostratigraphic information. Boxes indicate approximate ages for the sediment interval based on the K–Ar age, magnetic reversal M14, and biostratigraphic constraints above U6. The lithology log is from Kraus (2016). Grey vertical boxes show normal polarity zones of the geomagnetic polarity timescale. Wavy lines indicate inferred hiatuses. Black open circles = magnetic reversals for preferred LOC. Grey open circles = magnetic reversals for alternate LOCs. Blue triangles = dinoflagellate cyst bioevents. Red triangle = diatom bioevent. Yellow triangle = pollen bioevent. Black triangles = nannofossil bioevents. Red triangle = foraminifer bioevent. Green circles = strontium isotope ages. Pink circle = K–Ar glauconite age. Datum labels correspond to those in Table 1. Magnetic stratigraphy: black = normal polarity; white = reverse polarity; grey = not interpreted. Grey box between CSI 4 and CSI 3 indicates uncertainty in the CSI boundary placement. (For interpretation of the references to colour in this figure legend, the reader is referred to the web version of this article.)

and 240.75 mbsf. This section of core includes a zone of weakly stratified diamictite and sandy diamictite, overlain by sandstone and mudstone with rhythmically laminated silt layers that is highly characteristic of a glaciomarine setting proximal to an ice sheet grounding line and likely marks an episode of glacial advance into a shallow marine environment proximal to the site (Kraus, 2016). We correlate magnetozone R5 with C7r but suggest that much of the time represented by this chron is missing in a disconformity (U5) related to this glacial advance. We correlate magnetic reversal R5/N5 (MR6) with C7r/C7n.2n (24.474 Ma) and suggest that much of the time represented by Chron C7n.2n is missing across disconformity (U4), potentially related to a shift in base level due to the retreating ice masses as indicated by the laminated mudstone beneath this disconformity (Figs. 5 and 9). This inferred chronostratigraphic break occurs within the interval between 201 and 196 mbsf that is characterized by a sequence of muddy and sandy diamictite that grades into mudstone with dispersed clasts. The contact between each gradational unit is sharp (Kraus, 2016). This interval also coincides with a major change in foraminifer assemblage that includes a significant increase in agglutinated forms (Leckie and Webb, 1983). A major change in palynomorph content also occurs across this interval with protoperidinioid dinoflagellates replacing leiospheres as the dominant component. We correlate magnetic reversal N5/R6 (MR5) with C7n.1n/C6Cr (23.962 Ma) and suggest that most of the long reversed magnetozone R6 (the interval from 188.05 to 145.66 mbsf) corresponds to lower C6Cr. We constrain the slope of the LOC in this section of the model using MR5 and the base of Subchron C7n.1n but note the potential for a significant drop in sedimentation rate uphole in this interval, as the mudstone facies becomes finer grained and massive. Such facies are consistent with a glaciomarine setting distal to an ice sheet grounding line relative to the underlying laminated mudstone. Comparison of this sedimentary facies to modern glaciomarine environments indicates significant decreases in sedimentation rate as ice sheet grounding lines become more distal to a drill site (e.g., McKay et al., 2009).

5.1.3. CSI 3 (149–146 to 121/112 mbsf)

Sediments above U3 at the base of CSI 3 must be younger than the HO of *Dictyococcites bisectus* (CN1). This species is consistently present in samples that contain calcareous nannofossils below U3. The top of CSI 3 is defined by a sharp contact between a sandy siltstone and overlying sandy mudstone at 121.08 mbsf that coincides with a change in foraminifer assemblage composition and an increase in *Nothofagidites* pollen. We place disconformity U2 at this horizon based on the lithostratigraphy and fossil assemblage data mentioned above. However, a $^{87}\text{Sr}/^{86}\text{Sr}$ date on a shell fragment at 112.96 mbsf (S2) indicates that sediments at this horizon are 23.0 ± 0.3 Ma or older and the LO of *Batiacasphaera cooperi* (D4) at 111.13 mbsf indicates that sediments above this horizon are < 20.7 Ma. These datums suggest that a disconformity occurs at ~112 mbsf. A distinct dark grey mudstone with very rare clasts occurs between 112.54 and 112.68 mbsf and may represent a condensed interval. We acknowledge that the shell may have been reworked up-section from sediments below 121 mbsf. Regardless, the data indicate that ~2.5 million years of record is missing in the interval between 121 and 112 mbsf and suggest that sediments below U2 are older than 23 Ma. Based on the constraints outlined above we correlate the magnetic polarity reversal R6/N6 (MR4) to C6Cn.2r/C6Cn.2n (23.03 Ma), which places the Oligocene/Miocene boundary between 148.68 and 142.64 mbsf. However, we also note that the lower part of this interval (between 146 and 149 mbsf) corresponds to disconformity U3 and we cannot rule out that the Oligocene/Miocene boundary falls within this hiatus.

5.1.4. CSI 4 (121/112 to 20 mbsf)

A diatom-rich assemblage was recovered from a single sample at 105.00 mbsf and contains the age diagnostic taxon *Kisseleviella tricornata* (reported as *K. carina*) (Steinhauff et al., 1987). This species has

reported stratigraphic range of late Oligocene to early Miocene (C6An.2n) (Olney et al., 2005, 2007; Scherer et al., 2000) and indicates that sediments below 105.00 mbsf in DSDP Site 270 are > 20.439 Ma. The LO of *Batiacasphaera cooperi* (D4) at 93.20 mbsf indicates that sediments above this horizon are < 20.7 Ma. These two datums provide constraints that tie magnetozone N6 above U2 to Subchron C6An.2n. The highest occurrences of the dinoflagellates *B. cooperi* (D2) and *Lejeuncysta striata* (D1) at 57.14 and 27.30 mbsf, respectively, indicate that CSI 4 is early Miocene in age (18 to 20.7 Ma). We have low confidence in the magnetostratigraphy within CSI 4 due to poor core recovery and samples with lower than expected inclinations. However, based on these limited data, we tentatively interpret three magnetic polarity reversals (MR3, MR2, and MR1 in Fig. 9). If we then apply a simple LOC to this section, we can correlate magnetic reversals N6/R7 (MR3), R7/N7 (MR2), and N7/R8 (MR1) to C6An.2n/C6An.1r (20.439 Ma), C6An.1r/C6An.1n (20.213 Ma), and C6An.1n/C6r (20.04 Ma), respectively, which is consistent with ages provided by biostratigraphy.

5.2. Late Oligocene to early Miocene paleoenvironment

Our preferred age model indicates the DSDP Site 270 contains a stratigraphic sequence comprising ~250 m of upper Oligocene and ~130 m of lower Miocene sedimentary rocks, punctuated by six disconformities of varying duration. Upper Oligocene sediments from 450 to 200 mbsf are predominantly massive mudstone with dispersed to abundant clasts that contain rare pollen and common acritarchs. Except for one sample at 327.76 mbsf, calcareous nannofossils are very rare in this succession and mostly found in samples deeper than 280 mbsf. Foraminifers are also more abundant in the lower part of this succession and the best assemblages are preserved below 310 mbsf. Most samples above 310 mbsf are either barren of foraminifers or contain a few agglutinated forms or poorly preserved calcareous benthic species. Relatively abundant marine calcareous plankton and acritarchs coincide with sparse pollen in samples between ~345 and 245 mbsf and suggest these sediments were deposited in a predominantly grounding line distal, open marine setting (Fig. 5). Benthic foraminifer assemblages at the base of this succession (~345 mbsf) indicate a paleo-water depth of ~200 m. A 15-m thick interval of diamictite occurs between ~245 and 230 mbsf. The base of this succession is marked by a short unconformity (U5). These grounding line proximal sediments are barren of calcareous plankton and indicate that ice sheets had advanced into the marine environment and were grounded close to the drill site at 24.5 Ma. Benthic foraminifer assemblages in mudstone units above the diamictite indicate water depths of up to 500 m (Leckie and Webb, 1983, 1986). The presence of (rare) calcareous plankton and a decrease in IRD suggest ice retreated from the drill site between ~24.5 and 23.5 Ma. Given the absence of evidence for climatic warming in the Antarctic at this time (e.g., Roberts et al., 2003; Pekar et al., 2006; Prebble et al., 2006; Hauptvogel et al., 2017; Hartman et al., 2018), we infer this retreat was driven by basin subsidence (possibly resulting from ice growth on West Antarctica) and incursion of warm deep water across the continental shelf towards the West Antarctic continental interior.

We place the Oligocene/Miocene boundary between ~148 and 143 mbsf (Fig. 9). An increase in pollen abundance above 143 mbsf suggests a change in environmental conditions that may reflect an increase in vegetation at the coast due to climate shifts or a local change in ocean and/or atmospheric circulation that changed pollen or sediment delivery to the site. The pollen assemblages above 143 mbsf are dominated by spores and podocarps. Occurrences of calcareous nannofossils are sporadic between 145 and 120 mbsf, whereas foraminifers are somewhat more abundant. Benthic foraminifer assemblages suggest that the basin continued to deepen through this interval (Leckie and Webb, 1986). The sedimentary succession is generally finer grained through this interval and contains less IRD, which suggests a

glaciomarine setting distal to an ice sheet ground line.

The increase in *Nothofagidites* pollen relative abundance above 120 mbsf suggests climatic cooling into the early Miocene (Fig. 5). However, within the limitations of low numbers of pollen grains (especially for the upper Oligocene interval), the overall pollen assemblage shows minimal change in terrestrial climate over the late Oligocene to early Miocene interval at Site 270. Assemblage variability is like that seen in the upper Oligocene/lower Miocene of the CRP-2 cores, which is interpreted to represent tundra landscape that included low-growing *Nothofagus*, Podocarpaceae, and Proteaceae scrub in lower elevations/latitudes in the region (Prebble et al., 2006; Lewis et al., 2008).

5.3. Limitations of the revised chronostratigraphy

Development of robust age models in Antarctic sedimentary sequences that lack significant amounts of carbonate is challenging; however, here we combine age evidence from a variety of sources to develop a preferred age model. We also include two alternate age models that also fit within the constraints of the data (Fig. 9). The revised age model is based on significantly more data than originally available, but we note that the revised age model is still loosely constrained in some instances and therefore should be used with caution for precise dating (i.e., the error bars on the age model line of correlation are large).

Biostratigraphic datums are based on sparse microfossil assemblages. This is particularly true for calcareous nannofossils, which were only present in approximately 25% of examined samples. Even when present, nannofossils were mostly rare or extremely rare within the Site 270 sequences. No obviously out-of-place taxa were observed, so we do not think that contamination has affected our results. However, nannofossil biostratigraphy is based on the highest occurrences of three taxa. We cannot rule out that these occurrences are reworked, although the limited occurrences of nannofossils makes this less likely. Calcareous foraminifers are also rare and may suffer from similar issues.

Our preferred line of correlation relies on assignment of paleomagnetic reversals within the Site 270 sequence to the geomagnetic polarity timescale within the constraints provided by other chronostratigraphic datums. We note that samples deeper than ~185 mbsf show some form of gyro-remanence and therefore may be less reliable than samples from shallower in the sequence. For these samples the ChRMs were calculated using data points before the clear onset of gyro-remanence, which appeared at ~50 mT alternating field demagnetization. We are also less confident in the data above 100 mbsf due to the limited number of samples available because of poor core recovery, coupled with the lower than expected inclinations over that interval. While we tentatively interpret three magnetic reversals in this interval that fit a simple line of correlation, these data points should only be used with extreme caution.

Finally, we recognize that Sr-isotope results show significant scatter, although all ages fall within the range of ~23–27 Ma, which is consistent with other dating techniques. To help determine if any samples may have been compromised by post-depositional diagenesis, we measured minor and trace element composition of the wash solutions of samples. The results show elevated Mg/Ca for four samples; however, this does not confirm that the Sr-isotope data are bad, as the samples could have recrystallized from pore fluids that were similar to contemporaneous seawater. Regardless, due to the scatter and lack of coherency in the Sr-isotope age data, we place less weight on these results for development of the preferred age model.

6. Conclusions

Our revised age model for the upper Oligocene to lower Miocene marine sequence collected between 20 and 386 mbsf at DSDP Site 270 in the Ross Sea combines new biostratigraphy, magnetostratigraphy, Sr-

isotope stratigraphy, and radiometric dating. The sequence is divided into four CSIs:

1. CSI 1 (386 to 352 mbsf) is dated to 26–25 Ma, with the base of the sequence constrained by K–Ar dating of glauconite.
2. CSI 2 (352 to 149–146 mbsf) spans from ~25 Ma to 23 Ma, with the base marked by an unconformity (likely of short duration) based on a distinct change in the benthic foraminifer assemblage. This interval includes 7 paleomagnetic reversals tied to Chrons C8n.2n to C6Cr. Sedimentation was quite rapid (average of ~80 m/m.y.) during deposition of this unit. Benthic foraminifers indicate a paleowater depth of ~200 m near the base of the interval, deepening to ~500 m near the top. A package of diamictite between 245 and 230 mbsf indicates a more ice sheet grounding line proximal setting, which was followed by ice sheet grounding line retreat driven by basin subsidence and incursion of relatively warm deep water across the shelf.
3. CSI 3 (149–146 to 121/112 mbsf) is dated to around 23 Ma, and we place the Oligocene/Miocene boundary between 148 and 143 mbsf, just above the unconformity that marks the base of CSI 3. Benthic foraminifers indicate continued deepening, and fewer clasts in the fine-grained mudstone suggest an ice sheet grounding line distal setting, which may have been coupled with a decrease in sedimentation rate. The absence of calcareous plankton indicates deteriorating climatic conditions at that time.
4. The base of CSI 4 (121/112 to 20 mbsf) is marked by a hiatus of at least 2.5 m.y., with the base of the interval dated to ~20.7 Ma. The top of CSI 4 is a major unconformity that separates lower Miocene sediments from overlying Pliocene and younger sediments.

Paleobiological data suggest climate variability had an influence on ice sheet extent but also that crustal subsidence played a role in controlling marine ice sheet advance across the continental shelf. Pollen assemblages from Site 270 suggest a tundra landscape with low-growing *Nothofagaceae*, *Podocarpaceae*, and *Proteaceae* scrub persisted on the terrestrial landscape through most of the late Oligocene to early Miocene.

Supplementary data to this article can be found online at <https://doi.org/10.1016/j.gloplacha.2019.04.002>.

Acknowledgements

This work used archival Deep Sea Drilling Project samples and data provided by the International Ocean Discovery Program. This study was supported by the New Zealand Ministry of Business Innovation and Employment Contract C05X1001 (R.L., T.N., J.P., H.M., and C.C.) and Rutherford Discovery Fellowship (RDF-13_VUW-003) to R.M. Comments from Peter Bijl and one anonymous reviewer substantially improved the manuscript. We also thank Gary Acton for providing additional insight on the paleomagnetic interpretations. Many thanks to Randall McDonnell and Roger Tremain for processing samples for foraminifer, nannofossil, and palynomorph analysis. We also thank Dominic Strogen for examining the glauconite in thin section. Sookwan Kim kindly prepared the map figure.

References

- Allis, R.G., Barrett, P.J., Christoffel, D.A., 1975. A paleomagnetic stratigraphy for Oligocene and early Miocene marine glacial sediments at Site 270, Ross Sea, Antarctica. In: Hayes, D.E., Frakes, L.A. (Eds.), *Initial Reports of the Deep Sea Drilling Project*. vol. 28. U.S. Government Printing Office, Washington, pp. 879–884.
- Anson, G.L., Kodama, K.P., 1987. Compaction-induced inclination shallowing of the post-depositional remanent magnetization in a synthetic sediment. *Geophys. J. R. Astron. Soc.* 88, 673–692. <https://doi.org/10.1111/j.1365-246X.1987.tb01651.x>.
- Arndt, J.E., Schenke, H.W., Jakobsson, M., Nitsche, F.O., Buys, G., Goleby, B., Rebecso, M., et al., 2013. The International Bathymetric Chart of the Southern Ocean (IBCSO) Version 1.0—a new bathymetric compilation covering circum-Antarctic waters. *Geophys. Res. Lett.* 40 (12), 3111–3117. <https://doi.org/10.1002/grl.50413>.

- Askin, R.A., Raine, J.I., 2000. Oligocene and early Miocene terrestrial palynology of the Cape Roberts Drillhole CRP-2/2A, Victoria Land Basin, Antarctica. *Terra Antarct.* 7 (4), 493–501.
- Barrett, P.J., 2007. Cenozoic climate and sea level history from glaciomarine strata off the Victoria Land coast, Cape Roberts Project, Antarctica. In: Hambrey, M.J., Christoffersen, P., Glasser, N.F., Hubbard, B. (Eds.), *Glacial Sedimentary Processes and Products*. vol. 39. Special Publication of the International Association of Sedimentologists, pp. 259–288.
- Barrett, P.J., Hambrey, M.J., Robinson, P.R., 1991. Cenozoic glacial and tectonic history from CIROS-1, McMurdo Sound. *Int. Symp. Antarct. Earth Sci.* 5, 651–656.
- Bartek, L.R., Anderson, J.B., 1991. Facies distribution resulting from sedimentation under polar interglacial climatic conditions within a high-latitude margin basin, McMurdo Sound, Antarctica. *Special Paper – Geological Society of America* 261, 27–49. <https://doi.org/10.1130/SPE261-p27>.
- Bijl, P.K., Houben, A.J.P., Bruls, A., Pross, J., Sangiorgi, F., 2018. Stratigraphic calibration of Oligocene–Miocene organic-walled dinoflagellate cysts from offshore Wilkes Land, East Antarctica, and a zonation proposal. *J. Micropalaeontol.* 37, 105–138.
- Bonhomme, M., Thuizat, R., Pinault, Y., Clauer, N., Wendling, R., Winkler, R., 1975. Méthode de datation potassium-argon. *Appareillage et techniques*. Note Tech. Inst. Géol. Strasbourg, vol. 3, 1–53.
- Bown, P.R., 1998. *Calcareous Nannofossil Biostratigraphy*. Kluwer Academic, London (315pp).
- Bown, P.R., Young, J.R., 1998. Techniques. In: Bown, P.R. (Ed.), *Calcareous Nannofossil Biostratigraphy*. Kluwer Academic, London, pp. 16–28.
- Brancolini, G., Busetti, M., Marchetti, M., De Santis, L., Zanolla, C., Cooper, A.K., Conchane, G.R., Zayatz, I., Belyaev, V., Knyazev, M., Vinnikovskaya, O., Davey, F.J., Hinz, K., 1995. Seismic stratigraphic atlas of the Ross Sea, Antarctica. In: Cooper, A.K., Barker, P.F., Brancolini, G. (Eds.), *Antarctic Research Series (Vol. 68): Geology and Seismic Stratigraphy of the Antarctic Margin*. American Geophysical Union, Washington, DC.
- Bukry, D., 1975. Coccolith and silicoflagellate stratigraphy near Antarctica, Deep Sea Drilling Project, Leg 28. In: Hayes, D.E., Frakes, L.A. (Eds.), *Initial Reports of the Deep Sea Drilling Project*. vol. 28. U.S. Government Printing Office, Washington, pp. 709–723. <https://doi.org/10.2973/dsdp.proc.28.120.1975>.
- Burns, D.A., 1975. Nannofossil biostratigraphy for Antarctic sediments, Leg 28, Deep Sea Drilling Project. In: Hayes, D.E., Frakes, L.A. (Eds.), *Initial Reports of the Deep Sea Drilling Project*. vol. 28. U.S. Government Printing Office, Washington, pp. 589–598. <https://doi.org/10.2973/dsdp.proc.28.115.1975>.
- Chen, P.-H., 1975. Antarctic radiolaria. In: Hayes, D.E., Frakes, L.A. (Eds.), *Initial Reports of the Deep Sea Drilling Project*. vol. 28. U.S. Government Printing Office, Washington, pp. 437–513. <https://doi.org/10.2973/dsdp.proc.28.111.1975>.
- Clowes, C.D., Hannah, M.J., Wilson, G.J., Wrenn, J.H., 2016. Marine palynostratigraphy and new species from the Cape Roberts drill-holes, Victoria land basin, Antarctica. *Mar. Micropalaeontol.* 126, 65–84. <https://doi.org/10.1016/j.marmicro.2016.06.003>.
- Cody, R.D., Levy, R.H., Harwood, D.M., Sadler, P.M., 2008. Thinking outside the zone: high-resolution quantitative diatom biochronology for the Antarctic Neogene. *Palaeogeogr. Palaeoclimatol. Palaeoecol.* 260, 92–121. <https://doi.org/10.1016/j.palaeo.2007.08.020>.
- Cody, R., Levy, R., Crampton, J., Naish, T., Wilson, G., Harwood, D., 2012. Selection and stability of quantitative stratigraphic age models: Plio–Pleistocene glaciomarine sediments in the ANDRILL 1B drillcore, McMurdo Ice Shelf. *Glob. Planet. Chang.* 96–97, 143–156. <https://doi.org/10.1016/j.gloplacha.2012.05.017>.
- Cook, C.P., Hill, D.J., van de Fliet, T., Williams, T., Hemming, S.R., Dolan, A.M., Pierce, E.L., Escutia, C., Harwood, D., Cortese, G., Gonzales, J.J., 2014. Sea surface temperature control on the distribution of far-traveled Southern Ocean ice-rafted detritus during the Pliocene. *Paleoceanography* 29, 533–548. <https://doi.org/10.1002/2014PA002625>.
- Cooper, A.K., Barrett, P.J., Hinz, K., Traube, V., Leitchenkov, G., Stagg, H.M.J., 1991. Cenozoic prograding sequences of the Antarctic continental margin: a record of glacio-eustatic and tectonic events. *Mar. Geol.* 102 (1–4), 175–213. [https://doi.org/10.1016/0025-3227\(91\)90008-R](https://doi.org/10.1016/0025-3227(91)90008-R).
- Crundwell, M.P., Scott, G.H., Thrasher, G.P., 1994. Calibration of Paleobathymetry Indicators by Integrated Seismic and Paleontological Analysis of Foreset Sequences, Taranaki Basin, New Zealand. In: 1994 New Zealand Petroleum Conference Proceedings, pp. 169–178.
- De Santis, L., Anderson, J.B., Brancolini, G., Zayatz, I., 1995. Seismic record of late Oligocene through Miocene glaciation on the Central and Eastern Continental Shelf of the Ross Sea. In: Cooper, A.K., Barker, P.F., Brancolini, G. (Eds.), *Antarctic Research Series (Volume 68): Geology and Seismic Stratigraphy of the Antarctic Margin*. American Geophysical Union, Washington, DC, pp. 235–260. <https://doi.org/10.1029/AR068p0235>.
- De Santis, L., Prato, S., Brancolini, G., Lovo, M., Torelli, L., 1999. The eastern Ross Sea continental shelf during the Cenozoic: implications for the West Antarctic ice sheet development. *Glob. Planet. Chang.* 23 (1–4), 173–196. [https://doi.org/10.1016/S0921-8181\(99\)00056-9](https://doi.org/10.1016/S0921-8181(99)00056-9).
- DeConto, R.M., Pollard, D., 2016. Contribution of Antarctica to past and future sea-level rise. *Nature* 531, 591–597. <https://doi.org/10.1038/nature17145>.
- Dell, R.K., Fleming, C.A., 1975. Oligocene–Miocene bivalve Mollusca and other macrofossils from Sites 270 and 272 (Ross Sea), DSDP, Leg 28. In: Hayes, D.E., Frakes, L.A. (Eds.), *Initial Reports of the Deep Sea Drilling Project*. vol. 28. U.S. Government Printing Office, Washington, pp. 693–703. <https://doi.org/10.2973/dsdp.proc.28.118.1975>.
- Dunlop, D.J., 1979. On the use of Zijderveld vector diagrams in multicomponent paleomagnetic studies. *Phys. Earth Planet. Inter.* 20, 12–40.
- Egli, R., 2004a. Characterization of individual rock magnetic components by analysis of remanence curves. 2. Fundamental properties of coercivity distribution. *Phys. Chem. Earth* 29 (13–14), 851–867.
- Egli, R., 2004b. Characterization of individual rock magnetic components by analysis of remanence curves. 3. Bacterial magnetite and natural processes in lakes. *Phys. Chem. Earth* 29 (13–14), 869–884.
- Fielding, C.R., Browne, G.H., Field, B., Florindo, F., Harwood, D.M., Krissek, L.A., Levy, R.H., Panter, K.S., Passchier, S., Pekar, S.F., 2011. Sequence stratigraphy of the ANDRILL AND-2A drillcore, Antarctica: a long-term, ice-proximal record of early to mid-Miocene climate, sea-level and glacial dynamism. *Palaeogeogr. Palaeoclimatol. Palaeoecol.* 305 (1–4), 337–351. <https://doi.org/10.1016/j.palaeo.2011.03.026>.
- Florindo, F., Wilson, G.S., Roberts, A.P., Sagnotti, L., Verosub, K.L., 2005. Magnetostratigraphic chronology of a late Eocene to early Miocene glaciomarine succession from the Victoria Land Basin, Ross Sea, Antarctica. *Glob. Planet. Chang.* 45, 207–236.
- Golledge, N.R., Kowalewski, D.E., Naish, T.R., Levy, R.H., Fogwill, C.J., Gasson, E.G.W., 2015. The multi-millennial Antarctic commitment to future sea-level rise. *Nature* 526, 421–425. <https://doi.org/10.1038/nature15706>.
- Golledge, N.R., Thomas, Z.A., Levy, R.H., Gasson, E.G.W., Naish, T.R., McKay, R.M., Kowalewski, D.E., Fogwill, C.J., 2017. Antarctic climate and ice-sheet configuration during the early Pliocene. *Clim. Past* 13, 959–975. <https://doi.org/10.5194/cp-13-959-2017>.
- Gradstein, F., Ogg, J., Schmitz, M., Ogg, G., 2012. In: Gradstein, F., Ogg, J., Schmitz, M., Ogg, G. (Eds.), *The Geologic Time Scale 2012*. Elsevier, Amsterdam, pp. 1144.
- Grommé, C.S., Wright, T., Peck, D., 1969. Magnetic properties and oxidation of iron-titanium oxide minerals in Alae Makaupiki lava lakes, Hawaii. *J. Geophys. Res.* 74, 5277–5293.
- Hartman, J.D., Sangiorgi, F., Salabarnada, A., Peterse, F., Houben, A.J.P., Schouten, S., Brinkhuis, H., Escutia, C., Bijl, P.K., 2018. Paleoclimatology and ice sheet variability offshore Wilkes Land, Antarctica – part 3: insights from Oligocene–Miocene TEX₈₆-based sea surface temperature reconstructions. *Clim. Past* 14, 1275–1297. <https://doi.org/10.5194/cp-14-1275-2018>.
- Hassold, N.J.C., Rea, D.K., van der Pluijm, B.A., Parés, J.M., 2009. A physical record of the Antarctic Circumpolar current: late Miocene to recent slowing of abyssal circulation. *Palaeogeogr. Palaeoclimatol. Palaeoecol.* 275, 28–36. <https://doi.org/10.1016/j.palaeo.2009.01.011>.
- Hauptvogel, D.W., Pekar, S.F., Pincay, V., 2017. Evidence for a heavily glaciated Antarctica during the late Oligocene “warming” (27.8–24.5 Ma): stable isotope records from ODP Site 690. *Paleoceanography* 32, 384–396. <https://doi.org/10.1002/2016PA002972>.
- Hayes, D.E., Frakes, L.A., et al., 1975. Initial Reports of the Deep Sea Drilling Project. vol. 28. U.S. Government Printing Office, Washington, pp. 1007. <https://doi.org/10.2973/dsdp.proc.28.1975>.
- Hayward, B.W., 1986. A guide to paleoenvironmental assessment using New Zealand Cenozoic foraminiferal faunas. *N. Z. Geol. Surv. Rep. Pal* 109.
- Heitzzler, J.R., Dickinson, G.O., Herron, E.M., Pitman III, W.C., Le Pichon, X., 1968. Marine magnetic anomalies, geomagnetic field reversals and motions of the ocean floor and continents. *J. Geophys. Res.* 73, 2119–2136.
- Henrys, S.A., Buecker, C.J., Niessen, F., Bartek, L.R., 2001. Correlation of seismic reflectors with the CRP-3 drillhole, Victoria Land Basin, Antarctica. *Terra Antarct.* 8, 127–136.
- Heslop, D., McIntosh, G., Dekkers, M.J., 2004. Using time- and temperature-dependent Preisach models to investigate the limitations of modelling isothermal remanent magnetization acquisition curves with cumulative log Gaussian functions. *Geophys. J. Int.* 157, 55–63.
- Hess, J., Lippolt, H., 1994. Compilation of K–Ar measurements on HD-B1 standard biotite. In: *Phanerozoic Time Scale*. vol. 12. IUGS Subcomm, pp. 19–23 Bull. Filiais. Inform. On Geochrono.
- Hinz, K., Block, M., 1984. Results of geophysical investigations in the Weddell Sea and in the Ross Sea, Antarctica. *Proc. 11th World Petrol. Cong.* 11 (2), 79–91.
- Holbourn, A., Henderson, A.S., MacLeod, N., 2013. *Atlas of Benthic Foraminifera*. Wiley-Blackwell & Natural History Museum, pp. 642.
- Huck, C.E.T., van de Pliet, T., Bohaty, S.M., Hammond, S.J., 2017. Antarctic climate, Southern Ocean circulation patterns, and deep water formation during the Eocene. *Paleoceanography* 32, 674–691. <https://doi.org/10.1002/2017PA003135>.
- Jovane, L., Acton, G., Florindo, F., Verosub, K.L., 2008. Geomagnetic field behavior at high latitudes from a paleomagnetic record from Eltanin core 27–21 in the Ross Sea sector, Antarctica. *Earth Planet. Sci. Lett.* 267, 435–443.
- Jovane, L., Florindo, F., Bazylinski, D.A., Lins, U., 2012. Prismatic magnetite magnetosomes from cultivated *Magnetovibrio blakemorei* strain MV-1: a magnetic fingerprint in marine sediments? *Environ. Microbiol. Rep.* 4 (6), 664–668.
- Kaneps, A.G., 1975. Cenozoic planktonic foraminifera from Antarctic deep-sea sediments, Leg 28, DSDP. In: Hayes, D.E., Frakes, L.A. (Eds.), *Initial Reports of the Deep Sea Drilling Project*. vol. 28. U.S. Government Printing Office, Washington, pp. 573–583. <https://doi.org/10.2973/dsdp.proc.28.113.1975>.
- Kemp, E.M., 1975. Palynology of Leg 28 drill sites, Deep Sea Drilling Project. In: Hayes, D.E., Frakes, L.A. (Eds.), *Initial Reports of the Deep Sea Drilling Project*. vol. 28. U.S. Government Printing Office, Washington, pp. 599–623. <https://doi.org/10.2973/dsdp.proc.28.116.1975>.
- Kirschvink, J.L., 1980. The least-squares line and plane and the analysis of paleomagnetic data. *Geophys. J. R. Astron. Soc.* 62, 699–718.
- Kraus, C., 2016. Oligocene to Early Miocene Glaciomarine Sedimentation of the Central Ross Sea, and Implications for the Evolution of the West Antarctic Ice Sheet. Victoria University of Wellington, pp. 164 Unpublished MSc. Thesis.
- Kruiver, P.P., Passier, H.F., 2001. Coercivity analysis of magnetic phases in sapropel S1 related to variations in redox conditions, including an investigation of the S ratio. *Geochem. Geophys. Geosyst.* 2, 2001GC000181.
- Kruiver, P.P., Dekkers, M.J., Heslop, D., 2001. Quantification of magnetic coercivity

- components by the analysis of acquisition curves of isothermal remanent magnetization. *Earth Planet. Sci. Lett.* 189 (3–4), 269–276.
- Lear, C.H., Rosenthal, Y., Coxall, H.K., Wilson, P.A., 2004. Late Eocene to early Miocene ice sheet dynamics and the global carbon cycle. *Paleoceanography* 19, PA4015. <https://doi.org/10.1029/2004PA001039>.
- Leckie, R.M., Webb, P.-N., 1983. Late Oligocene–early Miocene glacial record of the Ross Sea, Antarctica: evidence from DSDP Site 270. *Geology* 11, 578–582.
- Leckie, R.M., Webb, P.-N., 1986. Late Paleogene and early Neogene foraminifers of Deep Sea Drilling Project Site 270, Ross Sea, Antarctica. In: Kennett, J.P., von der Borch, C.C. (Eds.), *Initial Reports of the Deep Sea Drilling Project*. vol. 90. U.S. Government Printing Office, Washington, pp. 1093–1142.
- Lewis, A.R., Marchant, D.R., Ashworth, A.C., Hedenaes, L., Hemming, S.R., Johnson, J.V., Leng, M.J., Machlus, M.L., Newton, A.E., Raine, J.J., Willenbring, J.K., Williams, M., Wolfe, A.P., 2008. Mid-Miocene cooling and the extinction of tundra in continental Antarctica. *Proc. Natl. Acad. Sci. U. S. A.* 105 (31), 10676–10680.
- Li, Y.X., Wang, S., Fu, S., Jiao, W., 2014. Recognizing the threshold magnetic anisotropy for inclination shallowing: implications for correcting inclination errors of sedimentary rocks. *Front. Earth Sci.* 2 (8), 1–17. <https://doi.org/10.3389/feart.2014.00008>.
- Liewig, N., Clauer, N., Sommer, F., 1987. Rb-Sr and K-Ar dating of clay diagenesis in Jurassic sandstone oil reservoir, North Sea. *AAPG Bull.* 71, 1467–1474.
- Liu, C., Olsson, R.K., Huber, B.T., 1998. A benthic paleohabitat for *Præpararotalia* gen. Nov. and *Antarcticella* Loeblich and Tappan. *J. Foraminif. Res.* 28 (1), 3–18.
- Lurcock, P.C., Wilson, G.S., 2012. PuffinPlot: a versatile, user-friendly program for paleomagnetic analysis. *Geochem. Geophys. Geosyst.* 13, Q06Z45. <https://doi.org/10.1029/2012GC004098>.
- McArthur, J.M., 1994. Recent trends in strontium isotopes stratigraphy. *Terra Nova* 6, 331–358.
- McArthur, J.M., Howarth, R.J., Shields, G.A., 2012. Strontium isotope stratigraphy. In: Gradstein, F.M., Ogg, J.G., Schmitz, M.D., Ogg, G.M. (Eds.), *The Geologic Time Scale 2012*. Elsevier, pp. 127–144.
- McCormell, D.W., 1975. Diatom stratigraphy of the Southern Ocean. In: Hayes, D.E., Frakes, L.A. (Eds.), *Initial Reports of the Deep Sea Drilling Project*. vol. 28. U.S. Government Printing Office, Washington, pp. 515–571. <https://doi.org/10.2973/dsdp.proc.28.112.1975>.
- McDougall, I., 1977. Potassium-argon dating of glauconite from a greensand drilled at Site 270 in the Ross Sea, DSDP Leg 28. In: Barker, P.F., Dalziel, I.W.D. (Eds.), *Initial Reports of the Deep Sea Drilling Project*. vol. 36. U.S. Government Printing Office, Washington, pp. 1071–1072. <https://doi.org/10.2973/dsdp.proc.36.281.1977>.
- McDougall, I., Roksandic, Z., 1974. Total fusion $^{40}\text{Ar}/^{39}\text{Ar}$ ages using HIFAR reactor. *J. Geol. Soc. Aust.* 21, 81–89.
- McKay, R.M., Browne, G., Carter, L., Cowan, E., Dunbar, G., Krissek, L., Naish, T., Powell, R., Reed, J., Talarico, F., Wilch, T., 2009. The stratigraphic signature of the late Cenozoic Antarctic Ice Sheets in the Ross Embayment. *GSA Bull.* 121 (11/12), 1537–1561. <https://doi.org/10.1130/B26540.1>.
- Miller, K.G., Feigenson, M.D., Wright, J.D., Clement, B.M., 1991. Miocene isotope reference section, Deep Sea Drilling Project Site 608: an evaluation of isotope and biostratigraphic resolution. *Paleoceanography* 6 (1), 33–52.
- Mitra, R., Tauxe, L., 2009. Full vector model for magnetization in sediments. *Earth Planet. Sci. Lett.* 286, 535–545. <https://doi.org/10.1016/j.epsl.2009.07.019>.
- Naish, T.R., Woolfe, K.J., Barrett, P.J., Wilson, G.S., Atkins, C., Bohaty, S.M., Bücker, C.J., et al., 2001. Orbitally induced oscillations in the East Antarctic Ice Sheet at the Oligocene/Miocene boundary. *Nature* 413 (6857), 719–723. <https://doi.org/10.1038/35099534>.
- Naish, T., Powell, R., Levy, R., Wilson, G., Scherer, R., Talarico, F., Krissek, L., et al., 2009. Oblitely-paced Pliocene West Antarctic ice sheet oscillations. *Nature* 458 (7236), 322–328. <https://doi.org/10.1038/nature07867>.
- Odin, G.S., 35 collaborators, 1982. Interlaboratory standards for dating purposes. In: Odin, G.S. (Ed.), *Numerical Dating in Stratigraphy*, Part 1. John Wiley & Sons, Chichester, pp. 123–148.
- Ogg, J.G., 2012. Chapter 5 – Geomagnetic polarity time scale. In: Gradstein, F.M., Ogg, J.G., Schmitz, M.D., Ogg, G.M. (Eds.), *The Geologic Time Scale 2012*. Elsevier, pp. 85–113.
- Olney, M.P., Scherer, R.P., Bohaty, S.M., Harwood, D.M., 2005. Eocene–Oligocene paleoecology and the diatom genus *Kisseleviella* Sheshukova-Poretskaya from the Victoria Land Basin, Antarctica. *Mar. Micropaleontol.* 58, 56–72.
- Olney, M.P., Scherer, R.P., Harwood, D.M., Bohaty, S.M., 2007. Oligocene–early Miocene Antarctic nearshore diatom biostratigraphy. *Deep-Sea Research Part II: Topical Studies in Oceanography* 54, 2325–2349. <https://doi.org/10.1016/j.dsr2.2007.07.020>.
- Passchier, S., Krissek, L.A., 2008. Oligocene–Miocene Antarctic continental weathering record and paleoclimatic implications, Cape Roberts drilling Project, Ross Sea, Antarctica. *Paleogeogr. Palaeoclimatol. Palaeoecol.* 260, 30–40.
- Passchier, S., Browne, G., Field, B., Fielding, C.R., Krissek, L.A., Panter, K., Pekar, S.F., ANDRILL-SMS Science Team, 2011. Early and middle Miocene Antarctic glacial history from the sedimentary facies distribution in the AND-2A drill hole, Ross Sea, Antarctica. *Geol. Soc. Am. Bull.* 123 (11–12), 2352–2365. <https://doi.org/10.1130/B30334.1>.
- Patterson, M.O., McKay, R., Naish, T., Escutia, C., Jimenez-Espejo, F.J., Raymo, M.E., Meyers, S.R., Tauxe, L., Brinkhuis, H., IODP Expedition 318 Scientists, 2014. Orbital forcing of the East Antarctic ice sheet during the Pliocene and early Pleistocene. *Nat. Geosci.* 7, 841–847. <https://doi.org/10.1038/ngeo2273>.
- Pekar, S.F., DeConto, R.M., Harwood, D.M., 2006. Resolving a late Oligocene conundrum: deep-sea warming and Antarctic glaciation. *Paleogeogr. Palaeoclimatol. Palaeoecol.* 231, 29–40. <https://doi.org/10.1016/j.palaeo.2005.07.024>.
- Perch-Nielsen, K., 1985. Cenozoic calcareous nannofossils. In: Bolli, H.M., Saunders, J.B., Perch-Nielsen, K. (Eds.), *Plankton Stratigraphy*. Cambridge University Press, Cambridge, pp. 427–554.
- Persico, D., Fiorini, C., Villa, G., 2012. A refined calcareous nannofossil biostratigraphy for the middle Eocene–early Oligocene Southern Ocean ODP sites. *Paleogeogr. Palaeoclimatol. Palaeoecol.* 335–336, 12–23. <https://doi.org/10.1016/j.palaeo.2011.05.017>.
- Pollard, D., DeConto, R.M., Alley, R.B., 2015. Potential Antarctic Ice Sheet retreat driven by hydrofracturing and ice cliff failure. *Earth Planet. Sci. Lett.* 412, 112–121. <https://doi.org/10.1016/j.epsl.2014.12.035>.
- Powell, R.D., Hambrey, M.J., Krissek, L.A., 1998. Quaternary and Miocene glacial and climatic history of the Cape Roberts drillsite region, Antarctica. *Terra Antarct.* 5, 341–351.
- Prebble, J.G., Raine, J.J., Barrett, P.J., Hannah, M.J., 2006. Vegetation and climate from two Oligocene glacioeustatic sedimentary cycles (31 and 24 Ma) cored by the Cape Roberts Project, Victoria Land Basin, Antarctica. *Paleogeogr. Palaeoclimatol. Palaeoecol.* 231, 41–57.
- Roberts, A.P., Weaver, R., 2005. Multiple mechanisms of remagnetization involving sedimentary greigite (Fe_3S_4). *Earth Planet. Sci. Lett.* 231 (3–4), 263–277.
- Roberts, A.P., Wilson, G.S., Harwood, D.M., Verosub, K.L., 2003. Glaciation across the Oligocene–Miocene boundary in southern McMurdo Sound, Antarctica: new chronology from the CIROS-1 drill hole. *Paleogeogr. Palaeoclimatol. Palaeoecol.* 198, 113–130.
- Roberts, A.P., Chang, L., Heslop, D., Florindo, F., Larrasoana, J.C., 2012. Searching for single domain magnetite in the “pseudo-single-domain” sedimentary haystack: implications of biogenic magnetite preservation for sediment magnetism and relative paleointensity determinations. *J. Geophys. Res. Solid Earth* 117 (B8), B08104. <https://doi.org/10.1029/2012JB009412>.
- Robertson, D.J., France, D.E., 1994. Discrimination of remanence-carrying minerals in mixtures, using isothermal remanent magnetisation acquisition curves. *Phys. Earth Planet. Inter.* 82 (3–4), 223–234.
- Savage, M.L., Ciesielski, P.F., 1983. A revised history of glacial sedimentation in the Ross Sea region. In: Oliver, R.L., James, P.R., Jago, J.B. (Eds.), *Antarctic Earth Science. Proc. IV Int. Symposium of Antarctic Earth Science*, pp. 555–560.
- Scher, H.D., Bohaty, S.M., Smith, B.W., Munn, G.H., 2014. Isotopic interrogation of a suspected late Eocene glaciation. *Paleoceanography* 29, 638–644. <https://doi.org/10.1002/2014PA002648>.
- Scherer, R.P., Bohaty, S.M., Harwood, D.M., 2000. Oligocene and lower Miocene siliceous microfossil biostratigraphy of Cape Roberts Project Core CRP-2/2A, Victoria Land Basin, Antarctica. *Terra Antarct.* 7, 417–442.
- Shipboard Scientific Party, 1975. Sites 270, 271, 272. In: Hayes, D.E., Frakes, L.A. (Eds.), *Initial Reports of the Deep Sea Drilling Project*. vol. 28. U.S. Government Printing Office, Washington, pp. 211–334.
- Steiger, R.H., Jäger, E., 1977. Subcommittee on geochronology; convention on the use of decay constants in geo- and cosmochronology. *Earth Planet. Sci. Lett.* 36, 359–362.
- Steinhauff, D.M., Renz, M.E., Harwood, D.M., Webb, P.-N., 1987. Miocene diatom biostratigraphy of DSDP hole 272: stratigraphic relationship to the underlying Miocene of DSDP hole 270, Ross Sea. *Antarct. J. US* 22, 123–125.
- Stephenson, A., 1980. A gyroremanent magnetization in anisotropic magnetic material. *Nature* 284, 49–51.
- Tauxe, L., Steindorf, J.L., Harris, A., 2006. Depositional remanent magnetization: toward an improved theoretical and experimental foundation. *Earth Planet. Sci. Lett.* 244, 515–529. <https://doi.org/10.1016/j.epsl.2006.02.003>.
- Thompson, R., Oldfield, F., 1986. *Environmental Magnetism*. Allen and Unwin, London.
- van Morkhoven, F.P.C.M., Berggren, W.A., Edwards, A.S., 1986. Cenozoic cosmopolitan deep-water benthic foraminifera. *Bull. Centres Rech. Explor. Prod. Elf-Aquitaine Mem.* 11, 421.
- Verosub, K.L., 1977. Depositional and postdepositional processes in the magnetization of sediments. In: *Review of Geophysics and Space Physics*. vol. 15. pp. 129–143.
- Weiss, B.P., Kim, S.S., Kirschvink, J.L., Kopp, R.E., Sankaran, M., Kobayashi, A., Komeili, A., 2004. Ferromagnetic resonance and low-temperature magnetic tests for biogenic magnetite. *Earth Planet. Sci. Lett.* 224, 73–89.
- Wilson, G.S., Roberts, A.P., Verosub, K.L., Florindo, F., Sagnotti, L., 1998. Magnetobiostratigraphic chronology of the Eocene–Oligocene transition in the CIROS-1 core, Victoria Land margin, Antarctica: implications for Antarctic glacial history. *GSA Bull.* 110 (1), 35–47.
- Wilson, G.S., Bohaty, S., Fielding, C.R., Florindo, F., Hannah, M.J., Harwood, D.M., McIntosh, W.C., Naish, T.R., Roberts, A.P., Sagnotti, L., Scherer, R., Strong, C.P., Verosub, K.L., Villa, G., Watkins, D.K., Webb, P.-N., Woolfe, K., 2000. Chronostratigraphy of CRP-2/2A, Victoria Land Basin, Antarctica. *Terra Antarct.* 7 (4), 647–654.
- Wilson, G.S., Pekar, S.F., Naish, T.R., Passchier, S., DeConto, R., 2009. The Oligocene–Miocene boundary: Antarctic climate response to orbital forcing. *Dev. Earth Environ. Sci.* 8, 369–400. [https://doi.org/10.1016/S1571-9197\(08\)00009-8](https://doi.org/10.1016/S1571-9197(08)00009-8).
- Wilson, G.S., Levy, R.H., Naish, T.R., et al., 2012. Neogene tectonic and climatic evolution of the Western Ross Sea, Antarctica – chronology of events from the AND-1B drill hole. *Glob. Planet. Chang.* 96–97, 189–203. <https://doi.org/10.1016/j.gloplacha.2012.05.019>.
- Zachos, J.C., Flower, B.P., Paul, H., 1997. Orbitally paced climate oscillations across the Oligocene/Miocene boundary. *Nature* 388 (6642), 567–570. <https://doi.org/10.1038/41528>.
- Zijderveld, J.D.A., 1967. A.C. demagnetization of rocks. In: Collison, D.W., Creer, K.M., Runcorn, S.K. (Eds.), *Methods in Paleomagnetism*. Elsevier, Amsterdam, pp. 256–286.